Harmonics from a magic carpet

Thomas E. Dobra[1,2], Andrew G. W. Lawrie[1] † and Stuart B. Dalziel[2]

[1]Hele-Shaw Laboratory, University of Bristol, University Walk, Bristol, BS8 1TR, UK

[2]Department of Applied Mathematics and Theoretical Physics, University of Cambridge, Wilberforce Road, Cambridge, CB3 0WA, UK

(Received xx; revised xx; accepted xx)

We present a novel theoretical framework for the emission and absorption of two-dimensional internal waves in a density stratified medium. Our approach uses a weakly nonlinear perturbation expansion of a streamfunction field that exposes the harmonic structure emitted from a flexible boundary of infinite extent. We report the discovery of a special symmetry in polychromatic waves that share a common horizontal component of phase velocity. Under these conditions, there can be no wave-wave interactions in the domain interior, and therefore all harmonic generation is from the boundary. By activating polychromatic waves on this same flexible surface, we then consider the equivalent inverse problems of emission of a prescribed harmonic signature and absorption of wave energy from a given flow field. Specialising to monochromatic waves, to calculate the amplitudes and phases of the harmonics generated by a monochromatic boundary displacement and to find the explicit form of the absorbing boundary condition for a monochromatic internal wave, we present algorithms that refine lengthy algebraic processes down to a set of executable instructions valid for arbitrary order in the small parameter of the expansion. Finally, we compare our theoretical predictions up to third order with a sophisticated, digitally controlled experimental realisation that we call a "magic carpet", and we find that harmonic analysis of the flow field convincingly supports our theory.

1. Introduction

Internal waves provide one of the most important energy transmission systems on Earth: lunar diurnal excitation alone drives around 1 TW of wave power within the world's oceans (Egbert & Ray 2001). This energy causes, for example, the upwelling $2.5 \times 10^7\,\mathrm{m}^3\,\mathrm{s}^{-1}$ of dense, salty water from the deep ocean to the surface that forms part of sustaining the meridional overturning circulation (Nikurashin & Ferrari 2013). Without the ocean currents transporting heat from the equator towards the poles, much of western Europe would be profoundly colder. However, much remains to be understood about the generation mechanisms of internal waves. For example, van Haren *et al.* (2002) observed that the frequency spectrum in the deep ocean contains multiple peaks, of which only some correspond directly to the diurnal tide or wind-generated surface waves.

It is widely known that bodies oscillating at a single frequency, ω, at large amplitudes emit additional harmonics of frequency $n\omega$ $\left(n \in \mathbb{Z}_{\geqslant 2}\right)$, which could explain some of the peaks observed by van Haren *et al.*. In the laboratory, Mowbray & Rarity (1967) observed addtional harmonics when vertically oscillating a small cylinder with its axis horizontal, and Ermanyuk *et al.* (2011) produced them from a horizontally oscillating sphere. Furthermore, they are even generated by a quasi-monochromatic travelling sinusoidal boundary displacement (Mercier *et al.* 2010), for which linear theory predicts a single monochromatic internal wave. Thus, harmonics are necessarily a nonlinear phenomenon.

† Email address for correspondence: andrew.lawrie@bristol.ac.uk

Weakly nonlinear theory has been used to model the emission of additional wave beams arising from nonlinear processes. For example, at second order in the small perturbation parameter, Tabaei *et al.* (2005) predicted the second harmonic that is produced when an internal wave reflects off a rigid surface. In addition, Sutherland (2016) considered the generation of second harmonics arising from the interaction of bounded internal wave modes. Bourget *et al.* (2013) also used second-order analysis to predict the dominant pair of waves produced when triadic resonant instability splits an internal wave beam. Conversely, Ermanyuk *et al.* (2011) did not formally use a perturbation expansion to consider the higher harmonics emitted by a small horizontally oscillating sphere, but rather measured the experimental difference with the linear theory, for which they still found behaviours indicative of a weakly nonlinear regime.

With the exception of Ermanyuk *et al.* (2011), these examples only consider wave-wave interactions in an inviscid fluid. The oscillating sphere additionally permits nonlinear generation of waves at the boundary of the sphere. These are the only two possible generation mechanisms of additional harmonics in a laminar, inviscid flow. Introducing a turbulent boundary layer, which requires viscosity, would provide a notable third mechanism, which may also introduce other, non-harmonic frequencies (Clark & Sutherland 2010). For simplicity, here we only consider low- to moderate-amplitude displacements.

In this paper, we consider the comparatively straightforward boundary condition of a prescribed two-dimensional displacement about a flat, horizontal plane. This geometry is representative of a current flowing over an ocean basin and also of the surface of the ocean, where wind shear can generate internal waves (Pollard 1970). In the laboratory, this geometry is motivated by the "magic carpet" wave maker of Dobra *et al.* (2019) and also approximately applies to the wave generator of Gostiaux *et al.* (2007). We will use a weakly nonlinear perturbation expansion to calculate the harmonics produced by a horizontally phase-locked boundary displacement, and then to solve the inverse problem of determining the boundary displacement required to produce a given wave field, such as a monochromatic internal wave with no additional harmonics. This is dependent on the symmetry, which we will demonstrate in §3.3, that the harmonics are generated solely at the boundary for phase-locked inputs. To address the more general case where wave-wave interactions may occur, we have developed a method using Green's functions to calculate these interactions (Dobra 2018), and we expect to publish these aspects shortly.

This article is arranged as follows. First of all, we outline the weakly nonlinear perturbation expansion in §2. In §3, we present the process of calculating the harmonic spectrum for arbitrary horizontally phase-locked boundary displacements, including generalising d'Alembert's solution for a completely arbitrary linear waveform in §3.2. Then, we compare these predictions to experiments in §4. In §5, we repurpose the perturbation expansion to calculate the boundary displacement required to give a chosen flow field, which we exemplify for a monochromatic internal wave and verify experimentally. Finally, we summarise our findings in §6.

2. Approach

We develop a weakly nonlinear framework, in a similar vein to Tabaei *et al.* (2005), for two-dimensional, inviscid internal waves generated by a low-amplitude forcing of vertical displacement $h(x, t)$ along our wave maker, where $\mathbf{x} = (x, z)$ are the horizontal and vertically upwards coordinates, with $z = 0$ at the equilibrium height of the wave maker, and t is time. The waves propagate through a quiescent liquid with a linear, Boussinesq density stratification, $\rho_0(z)$, with no diffusion of mass or heat. Here, the buoyancy, or *Brunt-Väisälä*, frequency,

$$N = \sqrt{-\frac{g}{\rho_{00}} \frac{\mathrm{d}\rho_0}{\mathrm{d}z}}, \tag{2.1}$$

is constant, where g is the gravitational acceleration, ρ_{00} is the reference density and thus $\rho_0(z) = \rho_{00}\left(1 - \frac{N^2}{g} z\right)$. Furthermore, the Boussinesq approximation implies that the fluid is incompressible and thus does not admit acoustic waves (Sutherland 2010), thereby simplifying the following analysis. Let a be the dimensionless order of magnitude of the boundary forcing, h; for example, if h is a sinusoid of amplitude A and wavenumber k, then $a = Ak$. In the weakly nonlinear regime, $|a| \ll 1$, we will expand the governing equations and the boundary conditions in powers of a.

2.1. *Governing Equation*

Let $\mathbf{u}$ be the velocity field, p' the pressure perturbation from hydrostatic and ρ' the density perturbation from the background stratification, ρ_0. Then, the three nonlinear governing equations are the conservation of momentum (Euler equation),

$$\rho_{00}\left(\frac{\partial \mathbf{u}}{\partial t} + \mathbf{u} \cdot \nabla \mathbf{u}\right) = -\nabla p' - \rho' g \mathbf{e}_z, \tag{2.2}$$

the conservation of mass,

$$\frac{\partial \rho'}{\partial t} + \mathbf{u} \cdot \nabla(\rho_0 + \rho') = 0, \tag{2.3}$$

and the conservation of volume,

$$\nabla \cdot \mathbf{u} = 0. \tag{2.4}$$

We re-express these equations in terms of the buoyancy, $b = -\frac{g\rho'}{\rho_{00}}$, and the streamfunction, ψ, which is defined by $\mathbf{u} = \nabla \times (\psi \mathbf{e}_y) = \left(-\frac{\partial \psi}{\partial z}, \frac{\partial \psi}{\partial x}\right)$ and automatically satisfies volume conservation (2.4), thereby reducing the number of simultaneous scalar equations to solve from four to three.

Taking the curl of the momentum equation (2.2) and defining the Jacobian determinant,

$$\left|\frac{\partial(\alpha, \beta)}{\partial(x, z)}\right| = \frac{\partial \alpha}{\partial x}\frac{\partial \beta}{\partial z} - \frac{\partial \alpha}{\partial z}\frac{\partial \beta}{\partial x}, \tag{2.5}$$

which has the form and algebraic properties of the Poisson bracket in classical Hamiltonian dynamics, yields the vorticity equation,

$$\frac{\partial}{\partial t}\nabla^2\psi + \left|\frac{\partial\left(\psi, \nabla^2\psi\right)}{\partial(x, z)}\right| = \frac{\partial b}{\partial x}. \tag{2.6}$$

The quantity $-\nabla^2\psi$ is the vorticity, which points in the y direction for two-dimensional flows.

The conservation of mass (2.3) is transformed by simple substitution of variables,

$$\frac{\partial b}{\partial t} + \left|\frac{\partial(\psi, b)}{\partial(x, z)}\right| = -N^2\frac{\partial \psi}{\partial x}. \tag{2.7}$$

This formulation explicitly shows the buoyancy frequency, N, is intrinsic to the flows in a stratified fluid. All of the nonlinear terms are now contained in the two Jacobian determinants, which are the transformation of the advection operator, $\mathbf{u} \cdot \nabla$.

We expand the streamfunction, ψ, in powers of the small dimensionless amplitude, a,

$$\psi = a\psi_1 + a^2\psi_2 + a^3\psi_3 + \cdots = \sum_{n=1}^{\infty} a^n \psi_n, \tag{2.8}$$

and similarly for the buoyancy, b. For the following analysis, we assume that the coefficient functions $\psi_n(x, z, t)$ are no greater than ord(1), which is required for the sum to converge. Substitution of these expansions into the vorticity equation (2.6) gives

$$\frac{\partial}{\partial t}\nabla^2\left(\sum_{n=1}^{\infty} a^n\psi_n\right) + \left|\frac{\partial\left(\sum_{p=1}^{\infty} a^p\psi_p, \nabla^2\left(\sum_{q=1}^{\infty} a^q\psi_q\right)\right)}{\partial(x, z)}\right| = \frac{\partial}{\partial x}\left(\sum_{n=1}^{\infty} a^n b_n\right). \tag{2.9}$$

Setting $n = p + q$ in the Jacobian term and noting that $1 \leqslant p = n - q \leqslant n - 1$, so that the summation is now over n and p, enables factorisation to yield an outer sum in terms of powers of a,

$$\sum_{n=1}^{\infty} a^n \left\{\frac{\partial}{\partial t}\nabla^2\psi_n + \sum_{p=1}^{n-1}\left|\frac{\partial\left(\psi_p, \nabla^2\psi_{n-p}\right)}{\partial\left(x, z\right)}\right|\right\} = \sum_{n=1}^{\infty} a^n \frac{\partial b_n}{\partial x}. \tag{2.10}$$

Similarly, inserting the perturbation expansion (2.8) into the equation of conservation of mass (2.7) and summing over powers of a gives

$$\sum_{n=1}^{\infty} a^n \left\{N^2\frac{\partial\psi_n}{\partial x} + \sum_{p=1}^{n-1}\left|\frac{\partial\left(\psi_p, b_{n-p}\right)}{\partial\left(x, z\right)}\right|\right\} = -\sum_{n=1}^{\infty} a^n \frac{\partial b_n}{\partial t}. \tag{2.11}$$

Comparing coefficients of powers of a in the expanded governing equations (2.10) and (2.11) gives the two equations at ord (a^n),

$$\frac{\partial}{\partial t}\nabla^2\psi_n + \sum_{p=1}^{n-1}\left|\frac{\partial\left(\psi_p, \nabla^2\psi_{n-p}\right)}{\partial\left(x, z\right)}\right| = \frac{\partial b_n}{\partial x}, \tag{2.12a}$$

$$N^2\frac{\partial\psi_n}{\partial x} + \sum_{p=1}^{n-1}\left|\frac{\partial\left(\psi_p, b_{n-p}\right)}{\partial\left(x, z\right)}\right| = -\frac{\partial b_n}{\partial t}. \tag{2.12b}$$

The buoyancy at each order, b_n, can be eliminated by differentiating (2.12a) with respect to t and (2.12b) with respect to x and then adding the resulting equations to give the inhomogeneous internal wave equation for ψ_n,

$$\frac{\partial^2}{\partial t^2}\nabla^2\psi_n + N^2\frac{\partial^2\psi_n}{\partial x^2} = -\sum_{p=1}^{n-1}\left\{\frac{\partial}{\partial t}\left|\frac{\partial(\psi_p, \nabla^2\psi_{n-p})}{\partial(x, z)}\right| + \frac{\partial}{\partial x}\left|\frac{\partial(\psi_p, b_{n-p})}{\partial(x, z)}\right|\right\}. \tag{2.13}$$

The homogeneous part of this equation consists of the sum of two temporal derivatives and two spatial derivatives, so forms a wave equation. Its spatially anisotropic structure yields the unusual properties of internal waves. At first order ($n = 1$), the summation vanishes, leaving just the equation for linear internal gravity waves. For all higher order contributions to the streamfunction, the internal wave equation is inhomogeneous, but all terms in the summation arise from lower orders. Consequently, we can inductively evaluate all orders. This set of equations governs all weakly nonlinear wave-wave interactions in free space. However, especially in the case of a flow driven by a moving material surface, such as of our wave maker, it is necessary to consider in detail the role of boundary conditions.

2.2. *Boundary conditions*

The kinematic boundary condition on the wave maker is of no penetration. Since it is assumed inviscid, the fluid may slip along the boundary. Because the actuating rods of the wave maker move vertically, the velocity of its surface is in the vertical direction,

$$\mathbf{U}(x,t) = \frac{\partial h}{\partial t}\mathbf{e}_z. \tag{2.14}$$

No penetration of the boundary requires that the normal velocity of the fluid, in the direction of unit vector $\mathbf{n}$, matches that of the surface of the wave maker at $z = h(x,t)$,

$$\mathbf{u}\cdot\mathbf{n} = \mathbf{U}\cdot\mathbf{n}. \tag{2.15}$$

Let α be the angle the local tangent to the flexible wave maker surface makes with the horizontal, so that $\tan\alpha = \frac{\partial h}{\partial x}$, then using trigonometry, the normal vector pointing into the fluid can be expressed as $\mathbf{n} = (-\sin\alpha, \cos\alpha)$. Extracting a common factor of $\cos\alpha$, substituting into the boundary condition (2.15), expressing $\mathbf{u}$ in terms of ψ and $\mathbf{U}$ following (2.14), then written in the order $n_z u_z + n_x u_x = n_z U_z$, we obtain

$$\left.\frac{\partial\psi}{\partial x}\right|_{z=h} + \left.\frac{\partial h}{\partial x}\frac{\partial\psi}{\partial z}\right|_{z=h} = \frac{\partial h}{\partial t}. \tag{2.16}$$

A physical interpretation of this equation is that there is no penetration of the fluid material surfaces, $u_z = \frac{Dh}{Dt}$, where we have used the material (total) time derivative.

Solving partial differential equations on domains with time-varying, curved boundaries ($z = h$) is usually analytically intractable and here is no exception. Instead, under the low steepness approximation, $|a| \ll 1$, we Taylor expand the streamfunction about $z = 0$ with the summation variable q,

$$\sum_{q=0}^{\infty}\frac{h^q}{q!}\left(\frac{\partial}{\partial x} + \frac{\partial h}{\partial x}\frac{\partial}{\partial z}\right)\left.\frac{\partial^q\psi}{\partial z^q}\right|_{z=0} = \frac{\partial h}{\partial t}. \tag{2.17}$$

This expansion will be specialised and fully expanded in powers of a in §3.1 and §5.2 according to the configuration under consideration.

3. Evaluating harmonic spectra generated by boundary displacement

We develop a weakly nonlinear framework using the perturbation expansion introduced in §2 for evaluating the harmonic spectra for several classes of two-dimensional boundary displacement. We begin, in §3.1, by fully expanding the kinematic boundary condition and obtain a double summation over orders of a and a Taylor's expansion of the boundary. This summation can be condensed into a graph of dependencies where the flow moves from lower order to higher order solutions in the streamfunction variable. In §3.2, we go on to show d'Alembert's Solution for the linear wave equation in the general case of arbitrary spectra and phase relationships, and present the complementary evanescent solution, because higher harmonics at some point will fall into this category. We then make a specialisation, in §3.3, to horizontally phase-locked but otherwise arbitrary spectra, because this exhibits an interesting symmetry that we need to efficiently evaluate the special case of monochromatic displacements. The outcome of this algebra is a concise algorithm through which higher powers of sinusoids can be systematically converted into the higher harmonics, which we present in §3.4. Thus, we can uncover the relationships between harmonics and account for all the subharmonic contributions made by those higher harmonics.

3.1. *Boundary conditions*

In the weakly nonlinear regime, we assume that the prescribed boundary displacement, h is no greater than ord(a), so we define $\hat{h}$ = ord(1) such that $h = a\hat{h}$. In addition, we assume that the characteristics of the internal waves each only intersect the wave maker once, which requires $\max\left|\frac{\partial h}{\partial x}\right| < \min\cot\Theta$, where, as we will see in §3.2, Θ is the angle of the direction of energy propagation of one such internal wave to the vertical.

Then, we expand the streamfunction (2.8) in the kinematic boundary condition (2.16), collect terms of equal order (powers of a) and express as a double sum,

$$\sum_{q=0}^{\infty}\sum_{r=1}^{\infty}\frac{a^{q+r}}{q!}\hat{h}^q\left(\frac{\partial}{\partial x}+a\frac{\partial\hat{h}}{\partial x}\frac{\partial}{\partial z}\right)\frac{\partial^q\psi_r}{\partial z^q}\bigg|_{z=0}=a\frac{\partial\hat{h}}{\partial t}. \tag{3.1}$$

Now all quantities are either ord(1) or are powers of a, so this has been fully expanded. It is convenient to factor out powers of a and sum over them with summation variable n and use separate inner summations over q for each term. After adjusting the summation limits accordingly, we have

$$\sum_{n=1}^{\infty}a^n\left\{\sum_{q=0}^{n-1}\frac{\hat{h}^q}{q!}\frac{\partial^{q+1}\psi_{n-q}}{\partial x\,\partial z^q}\bigg|_{z=0}+\sum_{q=0}^{n-2}\frac{\hat{h}^q}{q!}\frac{\partial\hat{h}}{\partial x}\frac{\partial^{q+1}\psi_{n-q-1}}{\partial z^{q+1}}\bigg|_{z=0}\right\}=a\frac{\partial\hat{h}}{\partial t}. \tag{3.2}$$

The system is forced only at ord(a), so the right hand side contains no contributions for $n \geqslant 2$, and terms of those orders on the left hand side must themselves balance.

At ord(a^n), the $q = 0$ term in the first summation reduces to $\frac{\partial\psi_n}{\partial x}\Big|_{z=0}$. The remaining terms in the first q summation all arise from the Taylor's expansion that extrapolates evaluation of the vertical fluid velocity from $z = 0$ to the material surface at $z = h$. The second q summation contains corrections due to the variations of the surface normal, $\mathbf{n}$, about the vertical and these unavoidably contain the horizontal fluid velocity, which we also Taylor expand to extrapolate from $z = 0$ to $z = h$. Except for the $q = 0$ term in the first summation, which yields ψ_n, all terms that appear at ord(a^n) are contributions from lower orders. The forcing of the governing equation for ψ_n (2.13) also only depends on lower orders. Hence, as shown in figure 1, there exists a unidirectional cascade of dependence from lower to higher order streamfunction contributions.

In addition to the kinematic boundary condition (3.2), the solution must satisfy causality: the time-averaged energy flux must be directed away from $z \leqslant h$ for all components of the generated flow. For internal waves, this is equivalent to saying the group velocity has a positive vertical component. Let the time-average over one period of oscillation be denoted by angle brackets $\langle\cdot\rangle$. Then, causality requires $\langle p'w\rangle \geqslant 0$ for all linearly independent components of the flow (derived, for example, in Dobra 2018, pp. 143–144).

3.2. *D'Alembert's solution for arbitrary boundary displacements*

Setting $n = 1$ in the expansion of the governing equation (2.13) yields the first-order contribution to the streamfunction, ψ_1,

$$\frac{\partial^2}{\partial t^2}\nabla^2\psi_1+N^2\frac{\partial^2\psi_1}{\partial x^2}=0. \tag{3.3}$$

This is the linearised form of the wave equation for internal waves. As noted earlier, it has an anisotropic structure, and here we use a method of characteristics that generalises d'Alembert's solution to the classical wave equation (d'Alembert 1747). While a Fourier transform could be performed to obtain a dispersion relation directly, in general a Fourier

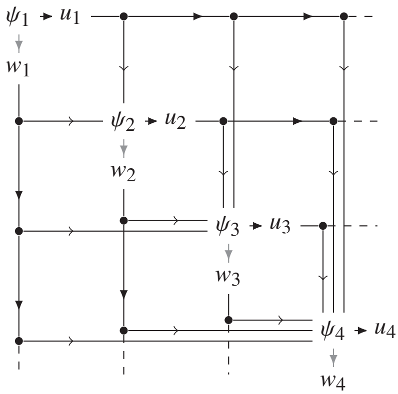

Figure 1: Graph of dependencies of contributions to the streamfunction at each order. The black triangular arrows indicate vertical (z) derivatives and grey triangular arrows indicate horizontal (x) derivatives. The other arrows only show the direction of dependence; no other operations occur.

approach cannot be used at higher orders containing quadratic Jacobian determinants, except for cases exhibiting a special symmetry, which we discovered and will report in §3.3. Furthermore, our approach identifies the hyperbolic structure and the geometry of the characteristics, which we have shown in Dobra (2018) is an important consideration for wave-wave interactions. The algebra given here is a preparatory step for extension to higher-order harmonics from a monochromatic boundary displacement, which we will discuss in §3.4.

The linear kinematic boundary condition is given by taking all terms of ord(a) in the expansion (3.2) ($n = 1,\ q = 0$),

$$\left.\frac{\partial \psi_1}{\partial x}\right|_{z=0} = \frac{\partial \hat{h}}{\partial t}. \tag{3.4}$$

We integrate this with respect to x,

$$\psi_1|_{z=0} = \int \frac{\partial \hat{h}}{\partial t}\,\mathrm{d}x, \tag{3.5}$$

where the arbitrary constant of integration will be chosen such that ψ represents the perturbation to the (constant) background streamfunction with no net volume flux through $z = 0$; in other words, $\left\langle \psi_1|_{z=0} \right\rangle = 0$.

Any smooth boundary displacement profile can be expressed as a real Fourier transform,

$$\hat{h} = \iint A(k,\omega)\sin(kx-\omega t) + B(k,\omega)\cos(kx-\omega t)\,\mathrm{d}\omega\,\mathrm{d}k, \tag{3.6}$$

where the functions A and B of k and ω are the Fourier coefficients. Substituting this form into the kinematic boundary condition (3.5) gives

$$\psi_1|_{z=0} = -\frac{\omega}{k}\iint A(k,\omega)\sin(kx-\omega t) + B(k,\omega)\cos(kx-\omega t)\,\mathrm{d}\omega\,\mathrm{d}k. \tag{3.7}$$

Since the operation of integration, the governing equation (3.3) and the boundary conditions are all linear, we will consider each term independently for a particular (k,ω) and then integrate over these contributions to recover the full streamfunction field.

Taking only the terms at a particular frequency ω, which we denote as ψ_ω, we seek a wave-like sinusoidal solution, so the linear internal wave equation reduces to the two-dimensional partial differential equation

$$-\omega^2\nabla^2\psi_\omega + N^2\frac{\partial^2\psi_\omega}{\partial x^2} = 0, \tag{3.8}$$

which readily rearranges into the form of the classical wave equation,

$$\left(\frac{N^2}{\omega^2} - 1\right)\frac{\partial^2\psi_\omega}{\partial x^2} - \frac{\partial^2\psi_\omega}{\partial z^2} = 0. \tag{3.9}$$

In the case $\omega > N$, this is an elliptic equation, so does not admit propagating wave solutions, but instead evanescent waves form, which we will discuss later in this section. Internal waves are the solutions that occur along characteristics when $\omega < N$ and thus the system is hyperbolic. Although elliptic equations can often be solved more readily than hyperbolic equations (for example, Hurley (1972) used analytic continuation to extend an elliptic solution to propagating internal waves), here we specialise d'Alembert's direct approach for the solution of hyperbolic forms (d'Alembert 1747) to linear internal waves. Solutions are projected along the characteristics, so satisfying the boundary condition at $z = 0$ provides a streamfunction everywhere in the fluid interior.

Factorising the hyperbolic differential operator yields

$$\left(\sqrt{\frac{N^2}{\omega^2} - 1}\frac{\partial}{\partial x} + \frac{\partial}{\partial z}\right)\left(\sqrt{\frac{N^2}{\omega^2} - 1}\frac{\partial}{\partial x} - \frac{\partial}{\partial z}\right)\psi_\omega = 0. \tag{3.10}$$

This form clearly shows the fundamental property of internal waves (when $\omega < N$) that the characteristics of the streamfunction, which are also the streamlines, are parallel at a constant angle to the vertical. Let Θ_1 be the angle these make with the vertical, where $0 < \Theta_1 < \frac{\pi}{2}$, and $\eta_{1\pm}$ be the normalised characteristic variables,

$$\eta_{1\pm} = x\cos\Theta_1 \pm z\sin\Theta_1. \tag{3.11}$$

The difference in η between two parallel characteristics is the perpendicular distance between them in (x, z) space. The derivatives with respect to $\eta_{1\pm}$ are found using the chain rule,

$$\frac{\partial}{\partial\eta_{1\pm}} = \sec\Theta_1\frac{\partial}{\partial x} \pm \operatorname{cosec}\Theta_1\frac{\partial}{\partial z} = \operatorname{cosec}\Theta_1\left(\tan\Theta_1\frac{\partial}{\partial x} \pm \frac{\partial}{\partial z}\right). \tag{3.12}$$

Comparing this with the factorised form of the wave equation (3.10) shows that

$$\frac{\partial^2\psi_\omega}{\partial\eta_{1+}\partial\eta_{1-}} = 0 \tag{3.13}$$

and $\tan\Theta_1 = \sqrt{\frac{N^2}{\omega^2} - 1}$, so

$$\omega = N\cos\Theta_1, \tag{3.14}$$

which we identify as the dispersion relation for linear internal waves. Therefore, the characteristics are parallel to the group velocity. Although the tangent function could take either sign, we take $\tan\Theta_1$ to be positive throughout this paper, because it represents a positive square root. The general solution of the transformed equation (3.13) is the sum of two arbitrary functions each of one variable,

$$\psi_\omega = f(\eta_{1+}) + g(\eta_{1-}). \tag{3.15}$$

Applying the boundary condition (3.7) at this chosen frequency, ω, to the general solution implies that this contribution to the streamfunction is of the form

$$\psi_\omega = -\frac{\omega}{k}\int CA\sin\left[k(x+z\tan\Theta_1)-\omega t\right]+(1-C)A\sin\left[k(x-z\tan\Theta_1)-\omega t\right] \\ +DB\cos\left[k(x+z\tan\Theta_1)-\omega t\right]+(1-D)B\cos\left[k(x-z\tan\Theta_1)-\omega t\right]\mathrm{d}k, \tag{3.16}$$

where C and D are constants to be determined from the causality condition, $\langle p_\omega w_\omega\rangle \geqslant 0$ on $z=0$. In fact, due to the characteristic nature of the system, this condition holds everywhere in the fluid domain, $z \geqslant 0$. The vertical velocity component w_ω is given by $\frac{\partial\psi_\omega}{\partial x}$, and we find the corresponding pressure perturbation by integrating the linearised horizontal momentum equation (2.2) with respect to x,

$$p_\omega = \rho_{00}\int \frac{\partial^2\psi_\omega}{\partial t\,\partial z}\,\mathrm{d}x, \tag{3.17}$$

where the integration constant will be set to zero to ensure zero time-averaged perturbation. Alternatively, one could derive this by considering the force balance on a fluid parcel; see Dobra (2018, p.144–145) for details. We now consider each sinusoid in turn, noting that time-averages of cross terms equal zero. For the first sinusoid,

$$\langle p_\omega w_\omega\rangle = C^2A^2\left\langle -\rho_{00}\frac{\omega k\tan\Theta_1}{k}k\cos^2\left[k(x+z\tan\Theta_1)-\omega t\right]\right\rangle = -\frac{1}{2}C^2A^2\rho_{00}k\omega\tan\Theta_1, \tag{3.18}$$

where we have used that the mean square of a sinusoid is half its amplitude. In preparation for considering phase-locked waves in §3.3, we define $c_x = \frac{\omega}{k}$ to be the horizontal phase velocity, and so

$$\langle p_\omega w_\omega\rangle = -\frac{1}{2}C^2A^2\rho_{00}k^2c_x\tan\Theta_1. \tag{3.19}$$

Causality is only satisfied for waves generated by the lower boundary when this quantity is positive, so $\sin\left[k(x+z\tan\Theta_1)-\omega t\right]$ is physical only when $c_x < 0$ (i.e. k and ω have opposite signs). Conversely, for the second sinusoid, the same method shows that $\langle p_\omega w_\omega\rangle = \frac{1}{2}(1-C)^2A^2\rho_{00}k^2c_x\tan\Theta_1$, so is only causal when $c_x > 0$. These properties hold for the third and fourth sinusoids, when the sine is replaced by a cosine, because it is simply a phase shift. Therefore, the coefficients C and D are either zero or one, according to the sign of the horizontal phase velocity. We succinctly express this using the sign function,

$$\psi_\omega = -\frac{\omega}{k}\int A(k,\omega)\sin\left[k(x-\operatorname{sgn}(k\omega)z\tan\Theta_1)-\omega t\right] \\ +B(k,\omega)\cos\left[k(x-\operatorname{sgn}(k\omega)z\tan\Theta_1)-\omega t\right]\mathrm{d}k. \tag{3.20}$$

Instead, if $\omega > N$, linear internal waves cannot propagate and are evanescent. Furthermore, the spatial equation (3.9) becomes elliptic, meaning that there are no real characteristics and information at one point propagates throughout the whole domain. We seek a separable solution, which we will denote ψ_e, that is harmonic in x, so must be exponential in z with growth/decay rate $k\sqrt{1-\frac{N^2}{\omega^2}}$. In order to satisfy causality, the disturbance decays into the fluid domain, so the contribution to the streamfunction in the evanescent case is

$$\psi_e = -\frac{\omega}{k}\int A(k,\omega)\,\mathrm{e}^{-kz\sqrt{1-\frac{N^2}{\omega^2}}}\sin(kx-\omega t)+B(k,\omega)\,\mathrm{e}^{-kz\sqrt{1-\frac{N^2}{\omega^2}}}\cos(kx-\omega t)\,\mathrm{d}k. \tag{3.21}$$

This is simply the (unstratified) potential flow response, but with a rescaled vertical coordinate, $z \mapsto z\sqrt{1-\frac{N^2}{\omega^2}}$; potential flow is smoothly recovered in the unstratified limit,

$N \to 0$. These forced oscillations are in phase with the boundary forcing. The disturbance extends further up into the fluid as the strength of the stratification increases and does not decay at all at the point where internal waves start to propagate, $N = \omega$. Unlike propagating internal waves, evanescent waves are reversible in time, meaning that it would not be possible to determine if a video of one is being played backwards. Thus, steady evanescent waves do not transport any energy.

Assembling the propagating (3.20) and evanescent (3.21) wave solutions gives the linear contribution to the streamfunction generated by an arbitrary boundary displacement expressed in the form (3.6),

$$\psi_1 = \int_{-\infty}^{-N} \psi_e \, \mathrm{d}\omega + \int_{-N}^{N} \psi_\omega \, \mathrm{d}\omega + \int_{N}^{\infty} \psi_e \, \mathrm{d}\omega. \tag{3.22}$$

3.3. *Symmetries of phase-locked internal waves*

Here, we derive a symmetry of phase-locked internal waves, both propagating and evanescent, which have the same horizontal phase velocity c_x. Such propagating waves may have an arbitrary amplitude spectrum according to

$$\psi = \int A(k) \sin\left[k(x - \mathrm{sgn}\,(c_x) z \tan\Theta - c_x t)\right] + B(k) \cos\left[k(x - \mathrm{sgn}\,(c_x) z \tan\Theta - c_x t)\right] \mathrm{d}k, \tag{3.23a}$$

where, from the dispersion relation (3.14), the angle $\Theta = \cos^{-1} \frac{k c_x}{N}$ and thus depends on k. The corresponding form of evanescent waves is

$$\psi = \int \mathrm{e}^{-kz\sqrt{1-\frac{N^2}{\omega^2}}} \Big(A(k) \sin\left[k(x - c_x t)\right] + B(k) \cos\left[k(x - c_x t)\right] \Big) \mathrm{d}k. \tag{3.23b}$$

This is a general description of travelling wavepackets of both finite and infinite extent along a material surface, such as the surface of the wave maker. This includes classes of problem such as atmospheric lee waves (e.g. Scorer 1949; Dalziel *et al.* 2011; Dobra *et al.* 2019), though excludes cases such as standing waves because they are superpositions of waves of opposing phase velocities. For such a propagating wave spectrum, the Jacobian terms (which correspond to the advection terms, $\mathbf{u} \cdot \nabla$, of the vorticity equation (2.6) and conservation of mass (2.7)) vanish. This important symmetry shows not only that resonant interactions in the domain interior are not admissible but in fact that all second-order interactions between waves arising from a horizontally phase-locked spectrum are inadmissible. We also note that, although linear, such a spectrum fully satisfies the nonlinear governing equations (2.2)–(2.4) at all amplitudes, which is a remarkable generalisation of this property observed for monochromatic plane waves by McEwan (1973) and Tabaei & Akylas (2003).

We now derive this symmetry by first differentiating the phase-locked form of the propagating streamfunction (3.23*a*) to obtain the negative of the vorticity,

$$\begin{aligned}\nabla^2 \psi_1 = -\int \Big(k^2 + k^2 \tan^2\Theta\Big) A(k) \sin\left[k(x - \mathrm{sgn}\,(c_x) z \tan\Theta - c_x t)\right] \\ + \Big(k^2 + k^2 \tan^2\Theta\Big) B(k) \cos\left[k(x - \mathrm{sgn}\,(c_x) z \tan\Theta - c_x t)\right] \mathrm{d}k.\end{aligned} \tag{3.24}$$

Using trigonometry and the dispersion relation (3.14) gives

$$k^2 + k^2 \tan^2\Theta = k^2 \sec^2\Theta = \frac{N^2}{c_x^2}, \tag{3.25}$$

which is a constant and so can be factored out of the integral. Therefore, the vorticity is proportional to the streamfunction with the constant of proportionality depending only on the buoyancy frequency, N, and the horizontal phase velocity, c_x,

$$\nabla^2\psi = -\frac{N^2}{c_x^2}\psi. \tag{3.26}$$

Applying the Laplacian to the evanescent form of the streamfunction (3.23*b*) gives the same result. From the linear and antisymmetric properties of Jacobians, we now show that the Jacobian corresponding to the vorticity is zero,

$$\left|\frac{\partial\left(\psi, \nabla^2\psi\right)}{\partial(x,z)}\right| = \left|\frac{\partial\left(\psi, -\frac{N^2}{c_x^2}\psi\right)}{\partial(x,z)}\right| = -\frac{N^2}{c_x^2}\left|\frac{\partial(\psi,\psi)}{\partial(x,z)}\right| = 0. \tag{3.27}$$

Similarly considering the buoyancy, b, each term in the integrand is a plane internal wave, which satisfies the linear internal wave equation (3.3), so we calculate the buoyancy for each component separately, denoted by a prime, using the linearised conservation of mass (2.6),

$$\frac{\partial b'}{\partial t} = -N^2\frac{\partial\psi'}{\partial x}, \tag{3.28}$$

and then integrate over the resulting contributions. For both propagating and evanescent waves, integrating mass conservation with respect to time gives $b' = \frac{N^2}{c_x}\psi'$, where the constant of integration has been set to zero to enforce zero average perturbation. Like the vorticity, the constant of proportionality is independent of the horizontal wavenumber, k, so may be factored out of the integral, yielding $b = \frac{N^2}{c_x}\psi$. Therefore, the Jacobian containing the buoyancy is also zero,

$$\left|\frac{\partial(\psi,b)}{\partial(x,z)}\right| = \frac{N^2}{c_x}\left|\frac{\partial(\psi,\psi)}{\partial(x,z)}\right| = 0, \tag{3.29}$$

and the symmetry of phase-locked internal waves is proven.

Consequently, for a phase-locked boundary displacement $\hat{h}$, the streamfunction contribution, ψ_n, is also phase-locked and thus is generated solely at the wave maker surface at all orders. We will now prove this using the strong principle of induction by first assuming that ψ_q is phase-locked with horizontal phase velocity c_x for all $q < n$. Then, the Jacobian terms in the expanded internal wave equation (2.13) at ord(a^n), which depend only on the lower, phase-locked orders, are all zero, so no wave-wave interactions can occur and the fluid response, ψ_n, is generated solely at the surface of the wave maker. The kinematic boundary condition (3.2) at ord(a^n) consists of $\left.\frac{\partial\psi_n}{\partial x}\right|_{z=0}$ and terms proportional to

$$\hat{h}^q\left.\frac{\partial^{q+1}\psi_{n-q}}{\partial x\,\partial z^q}\right|_{z=0} \quad \text{and} \quad \hat{h}^q\frac{\partial\hat{h}}{\partial x}\left.\frac{\partial^{q+1}\psi_{n-q-1}}{\partial z^{q+1}}\right|_{z=0},$$

which all sum to zero for $n \geqslant 2$, or $\frac{\partial\hat{h}}{\partial t}$ when $n = 1$. By the induction assumption, each of these terms is an integral over products of sines and cosines with uniform horizontal phase velocity c_x. The product of a pair of such sinusoids also has phase velocity c_x, because, for example,

$$\cos\left[A(x-c_xt)\right]\cos\left[B(x-c_xt)\right] = \frac{1}{2}\Big(\cos\left[(A+B)(x-c_xt)\right] + \cos\left[(A-B)(x-c_xt)\right]\Big), \tag{3.30}$$

where A and B are arbitrary constants, and thus all of the product terms in the kinematic boundary condition have horizontal phase velocity c_x. Therefore, integrating the boundary condition with respect to x and setting the integration constant to zero to ensure no net flux through $z = 0$ gives that $\psi_n|_{z=0}$ is also phase-locked. Since the Jacobian determinants are zero, the internal wave equation (2.13) at ord(a^n) reduces to the linear internal wave equation (3.3), and so, from the linear solution (3.20), the streamfunction contribution ψ_n is phase-locked everywhere in the domain. Finally, we already know from the linear solution that ψ_1 is phase-locked. Therefore, by induction, the streamfunction is phase-locked at all orders.

In general, the Jacobian determinant gives the area of the image of a unit element having undergone a coordinate transformation. Here, these zero Jacobian determinants indicate that the transformations into the two-dimensional streamfunction-buoyancy and streamfunction-vorticity spaces are singular for arbitrary superpositions of phase-locked internal waves, namely that all points map onto straight lines through the origin of gradients $\frac{N^2}{c_x}$ and $\frac{N^2}{c_x^2}$ respectively. Conversely, the image space remains two-dimensional for an unconstrained superposition of internal waves and other flows.

3.4. *Algorithmic evaluation of higher-order contributions for monochromatic boundary displacement*

We now present the process by which we obtain contributions to monochromatic boundary displacements for arbitrary order. The steps in this process we divide into a pair of interconnected algorithms 1 and 2, then for convenience we illustrate their use by explicitly calculating key expressions at first, second and third orders in tables 1–3.

In §3.3, we showed that the expansion of the internal wave equation (2.13) is linear at all orders for a phase-locked boundary displacement. A special case is of a monochromatic sinusoid travelling to the right, which is infinite in extent, $h = A\sin(kx - \omega t)$, where we use the convention $k, \omega > 0$. Defining the dimensionless amplitude as $a = Ak$, we have $\hat{h} = \frac{1}{k}\sin(kx - \omega t)$. For this case, we may derive analytic expressions for the produced spectrum of harmonics at each of the first three orders by noting that the flow at each order is only generated at the boundary. The expansion of the kinematic boundary condition (3.2) becomes

$$\sum_{n=1}^{\infty} a^n \left\{ \sum_{q=0}^{n-1} \frac{\sin^q \phi}{q!\,k^q} \left.\frac{\partial^{q+1}\psi_{n-q}}{\partial x\,\partial z^q}\right|_{z=0} + \sum_{q=0}^{n-2} \frac{\sin^q \phi\,\cos\phi}{q!\,k^q} \left.\frac{\partial^{q+1}\psi_{n-q-1}}{\partial z^{q+1}}\right|_{z=0} \right\} = -a\frac{\omega}{k}\cos\phi. \tag{3.31}$$

Since this condition at ord(a^n) depends on all of the lower orders, the contribution to the streamfunction at each order is evaluated in turn, according to algorithm 1.

To calculate the contribution to the streamfunction at ord(a^n), denoted by ψ_n, firstly we take the first n terms of the outer summation in (3.31). These are shown for the first three orders in table 1. The boundary condition at all orders contains $\left.\frac{\partial \psi_n}{\partial x}\right|_{z=0}$, which is the vertical velocity at ord(a^n). Higher orders also include derivatives of lower-order contributions to the streamfunction, and these are multiplied by sines and cosines of integer multiples of the horizontal phase, $\phi = kx - \omega t$. All derivatives are evaluated at the equilibrium height of the wave maker, $z = 0$. Secondly, we evaluate and substitute for the derivatives of the lower-order contributions to the streamfunction. For example, the required derivatives of ψ_1 follow the pattern

$$\left.\frac{\partial^{q+1}\psi_1}{\partial x\,\partial z^q}\right|_{z=0} = \begin{cases} (-1)^{\frac{q+2}{2}}\omega k^{q-1}\tan^q\Theta_1\,\cos\phi & \text{for even } q \\ (-1)^{\frac{q+1}{2}}\omega k^{q-1}\tan^q\Theta_1\,\sin\phi & \text{for odd } q \end{cases}, \tag{3.32a}$$

Result: ψ

$\psi \leftarrow 0$
for $n \in \mathbb{N}$ **do**
  Evaluate kinematic boundary condition (3.31) at ord(a^n)
  for $p \leftarrow 1$ **to** $n-1$ **do**
    Evaluate $\left.\frac{\partial^{q+1}\psi_p}{\partial x\,\partial z^q}\right|_{z=0}$ and $\left.\frac{\partial^{q}\psi_p}{\partial z^q}\right|_{z=0}$, $q < n$, following the pattern of (3.32)
    Express the terms as products of $\sin\phi$ and $\cos\phi$ using (3.33)
    Express these products as sums of harmonics using ALGORITHM 2
  end
  Collect like terms
  Integrate ψ_n with respect to x, setting the integration constant to zero
  for $p \leftarrow 1$ **to** n **do**
    if $p\omega \leqslant N$ **then**
      Project the $p\omega$ harmonic along its characteristics using (3.20)
    else
      Project the $p\omega$ harmonic as an evanescent wave into $z \geqslant 0$ using (3.21)
    end
  end
  $\psi \leftarrow \psi + a^n\psi_n$
end

ALGORITHM 1. Calculation of streamfunction ψ.

Order	Kinematic boundary condition at n^{th} order		
1st	$\left.\frac{\partial\psi_1}{\partial x}\right\|_{z=0}$	$=$	$-\frac{\omega}{k}\cos\phi$
2nd	$\left.\frac{\partial\psi_2}{\partial x}\right\|_{z=0} + \frac{1}{k}\sin\phi\left.\frac{\partial^2\psi_1}{\partial x\partial z}\right\|_{z=0} + \cos\phi\left.\frac{\partial\psi_1}{\partial z}\right\|_{z=0}$	$=$	0
3rd	$\left.\frac{\partial\psi_3}{\partial x}\right\|_{z=0} + \frac{1}{k}\sin\phi\left.\frac{\partial^2\psi_2}{\partial x\partial z}\right\|_{z=0} + \frac{1}{2k^2}\sin^2\phi\left.\frac{\partial^3\psi_1}{\partial x\partial z^2}\right\|_{z=0} + \cos\phi\left.\frac{\partial\psi_2}{\partial z}\right\|_{z=0} + \frac{1}{k}\sin\phi\cos\phi\left.\frac{\partial^2\psi_1}{\partial z^2}\right\|_{z=0}$	$=$	0

Table 1: Kinematic boundary condition at the first three orders for a monochromatic boundary displacement.

and

$$\left.\frac{\partial^{q+1}\psi_1}{\partial z^{q+1}}\right|_{z=0} = \tan\Theta_1 \left.\frac{\partial^{q+1}\psi_1}{\partial x\,\partial z^q}\right|_{z=0}. \tag{3.32b}$$

We are left with a product of sines and cosines of several multiples of ϕ for each term in the boundary condition. The next stage is to simplify these as sums of harmonics, or equivalently express a Fourier series, using the formulae derived using standard methods in appendix A. We first expand all of the higher harmonic terms into powers of trigonometric functions of

Result: S

for $j = 0$ **to** $\alpha + \beta$ **do**
  $C[j] \leftarrow 0$
  if $j \equiv \alpha + \beta \pmod 2$ **then**
    $B \leftarrow \max\left\{\frac{1}{2}(\beta - \alpha - j), 0\right\}$
    if $j = 0$ **then** $T \leftarrow \frac{\beta}{2} - 1$ **else** $T \leftarrow \min\left\{\frac{1}{2}(\beta + \alpha - j), \beta\right\}$
    for $k = B$ **to** T **do**
      $$C[j] \leftarrow C[j] + \frac{(-1)^{\left\lfloor \frac{\beta}{2} \right\rfloor + k}}{2^{\alpha+\beta-1}} \binom{\alpha}{\frac{1}{2}(\alpha + \beta - j) - k} \binom{\beta}{k}$$
    end
  end
end

if α *even* **and** β *even* **then** $C[0] \leftarrow C[0] + \dfrac{1}{2^{\alpha+\beta}} \dbinom{\alpha}{\frac{\alpha}{2}} \dbinom{\beta}{\frac{\beta}{2}}$

if β *even* **then** $S \leftarrow \displaystyle\sum_{j=0}^{\alpha+\beta} C[j] \cos(j\phi)$ **else** $S \leftarrow \displaystyle\sum_{j=0}^{\alpha+\beta} C[j] \sin(j\phi)$

ALGORITHM 2. Expressing $\cos^{\alpha}\phi \sin^{\beta}\phi$ as a sum of harmonics.

the fundamental using, for $p \in \mathbb{Z}$,

$$\cos(p\phi) = \sum_{\beta=0}^{\frac{p}{2}} (-1)^{\beta} \binom{p}{2\beta} \cos^{p-2\beta}\phi \sin^{2\beta}\phi \tag{3.33a}$$

and

$$\sin(p\phi) = \sum_{\beta=0}^{\frac{p-1}{2}} (-1)^{\beta} \binom{p}{2\beta+1} \cos^{p-2\beta-1}\phi \sin^{2\beta+1}\phi, \tag{3.33b}$$

where $\binom{n}{r}$ is the binomial coefficient. Then, we collect the terms into a single product and expand as a series of harmonics using formula (A 15), which we re-express for convenience as algorithm 2. Collecting like terms shows that $\left.\frac{\partial \psi_n}{\partial x}\right|_{z=0}$ is equal to a sum of harmonics with constant amplitudes. Moreover, we find that these harmonics need to be represented by cosine functions in order to match the symmetry of the boundary displacement about $x = 0$, and up to the n^{th} harmonic, denoted by $n\phi$, is included. For odd n, all and only the odd-numbered harmonics are present (up to the n^{th} harmonic); conversely, for even n, we have all and only even-numbered harmonics.

Such a form is readily integrated with respect to x to give the contribution to the streamfunction, ψ_n, evaluated at $z = 0$. We find that it is equal to a sum of sinusoids of phase $n\phi$. The integration constant is set to zero to enforce that the equilibrium height of the wave maker is at $z = 0$.

Since the streamfunction is a discrete sum of linearly independent temporal (and spatial) harmonics along the boundary and it satisfies the linear internal wave equation (3.3), we project each harmonic with a frequency less than the buoyancy frequency along the corresponding characteristics, which are at angle Θ_n to the vertical, given by the dispersion relation (3.14). Then, each harmonic takes the form of the linear solution (3.20). The harmonics above the buoyancy frequency generate evanescent waves, whose contribution

Order	Contribution to the streamfunction, ψ_n
1$^{\text{st}}$	$-\dfrac{\omega}{k^2}\sin\left[k(x - z\tan\Theta_1) - \omega t\right]$
2$^{\text{nd}}$	$-\dfrac{\omega}{2k^2}\tan\Theta_1\sin\left[2k(x - z\tan\Theta_2) - 2\omega t\right]$
3$^{\text{rd}}$	$\dfrac{\omega}{8k^2}\tan\Theta_1\left\{(\tan\Theta_1 - 4\tan\Theta_2)\sin\left[3k(x - z\tan\Theta_3) - 3\omega t\right] + (4\tan\Theta_2 - 3\tan\Theta_1)\sin\left[k(x - z\tan\Theta_1) - \omega t\right]\right\}$

Table 2: Contributions to the streamfunction at the first three orders, provided $3\omega < N$.

takes the form of the linear evanescent waves (3.21), with k and ω multiplied by the appropriate value of n. Finally, the contribution to the streamfunction, ψ_n, is given by the linear superposition of these propagating and evanescent internal waves, even though the solution is nonlinear. Provided the third harmonic is not evanescent, these contributions are listed in table 2 and are plotted in figure 2 together with a phase plot in physical space. We note that in this case all harmonics are in phase with the boundary displacement.

The leading-order contribution to the n^{th} harmonic comes from n^{th} order and so grows as a^n. Higher-order corrections to this harmonic arise at orders $(n+2)$, $(n+4)$, $(n+6)$, ..., but these corrections become decreasingly significant as a reduces. All of the corrections to the lower harmonics are also given by sine functions, thereby ensuring odd symmetry about $x = 0$. Considering the expression $4\tan\Theta_2 - 3\tan\Theta_1$ as a function of ω shows that the third-order correction to the first harmonic reinforces its amplitude for $0 < \omega < \frac{N}{2}$, and this reinforcement is more pronounced for smaller ω. Superlinear growth has been observed previously in experiments (Ermanyuk *et al.* 2017); here, in figure 2(*a*), we find it appearing on all three propagating harmonics within and beyond the domain of applicability ($kA < \cot\Theta_1$) in which each internal wave characteristic intersects the sinusoidal boundary exactly once.

Since each mode satisfies the linear equation (3.3), the energy density of each mode is proportional to the square of the amplitude with uniform constant of proportionality $\frac{1}{2}\rho_{00}N^2$ for all harmonics, and their time-averaged energy fluxes ($\langle p'|\mathbf{u}|\rangle$) are equal to their energy densities multiplied by their group velocities, which are given by $c_x \sin\Theta_n$. Although product terms are developed for all pairs of harmonics in the series, by orthogonality, the time averages of the cross terms are zero, leaving only the linear contributions for each mode. Thus, the energy density and the energy flux have very similar profiles, and as an illustration, we show the energy flux in figure 2(*b*). We see that for a given monochromatic input, the total energy flux is greater than that contained in the single wave beam predicted by the linear theory. The increased energy flux is not a violation of causality, because the power that the flexible boundary transmits to the fluid is not specified, only the position of its surface.

On the other hand, if at least one of the first three harmonics were evanescent ($3\omega > N$), some of the tangent functions would be replaced by explicit square roots, $\tan\Theta_n = \sqrt{\left(\frac{N}{n\omega}\right)^2 - 1} \mapsto \sqrt{1 - \left(\frac{N}{n\omega}\right)^2}$, as can be seen in the linear evanescent solution (3.21). Moreover, the z derivatives of an evanescent wave have a different phase to those of the corresponding propagating wave, so if the m^{th} harmonic is the lowest evanescent one, all contributions at $(m+1)^{\text{th}}$ and higher orders become phase-shifted relative to the boundary displacement. For any given order of perturbation expansion, the explicit form of the solution depends on the number of propagating harmonics, and we provide up to the third-order

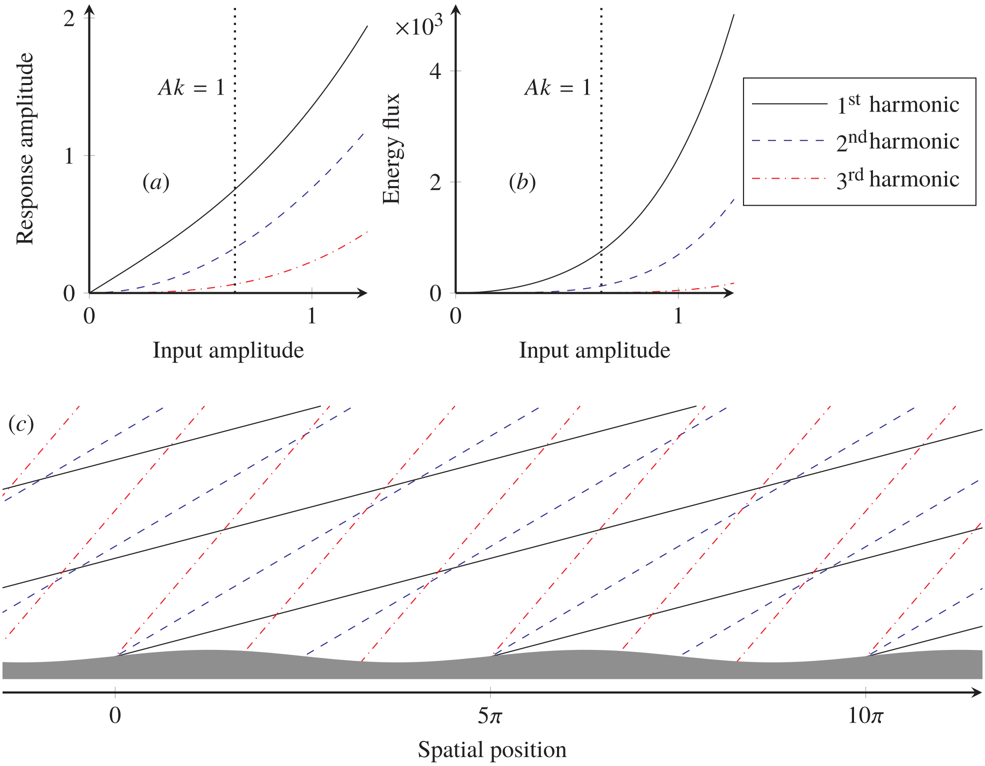

Figure 2: Predictions for the first three harmonics generated by an input sinusoid of frequency $\omega = 0.4 = 0.25N$ and wavenumber $k = 0.4$, where units for frequency and wavenumber are freely chosen provided they are self-consistent: (a) vertical displacement amplitude; (b) time-averaged energy flux, which has a similar profile to the energy density; and (c) phase profile showing the characteristics where ψ decreases through zero, equivalently where the vertical displacement increases through zero. The expansion is valid for $Ak < 1$, since thereafter some of the characteristics will intersect the flexible boundary more than once.

contributions in table 3 for when only the first harmonic is propagating. In this case, the first three harmonics again grow superlinearly.

4. Experimental validation

This section presents a sequence of experiments conducted to verify the predictions made in §3.4 for the fluid response to monochromatic displacement of a flexible boundary. In §4.1, we briefly describe the "magic carpet" used to provide these displacements, and the reader is referred to Dobra *et al.* (2019) for a more detailed discussion and validation of the apparatus. The following section, §4.2, outlines our data acquisition pipeline from raw camera images to estimates of the amplitude of each harmonic. Finally, we present a detailed comparison between the predicted and observed amplitudes of each harmonic in §4.3.

4.1. *Magic carpet*

The Arbitrary Spectrum Wave Maker (ASWaM, Dobra *et al.* 2019) is a 1 m-long, flexible section in the base of an 11 m-long tank that is 0.255 m wide and 0.48 m deep. The wave maker's shape is controlled by an array of 100 Portescap 26DBM10D1B-L linear stepper

Order	Contribution to the streamfunction, ψ_n
1^{st}	$-\dfrac{\omega}{k^2}\sin\left[k(x - z\tan\Theta_1) - \omega t\right]$
2^{nd}	$-\dfrac{\omega}{2k^2}\tan\Theta_1\,\mathrm{e}^{-2kz\sqrt{1-\left(\frac{N}{2\omega}\right)^2}}\sin\left[2kx - 2\omega t\right]$
3^{rd}	$\dfrac{\omega}{8k^2}\tan\Theta_1\left\{\left(\tan\Theta_1\sin\left[3kx - 3\omega t\right] + 4\sqrt{1-\left(\dfrac{N}{2\omega}\right)^2}\cos\left[3kx - 3\omega t\right]\right)\mathrm{e}^{-3kz\sqrt{1-\left(\frac{N}{3\omega}\right)^2}} - 3\tan\Theta_1\sin\left[k(x - z\tan\Theta_1) - \omega t\right] - 4\sqrt{1-\left(\dfrac{N}{2\omega}\right)^2}\cos\left[k(x - z\tan\Theta_1) - \omega t\right]\right\}$

Table 3: Contributions to the streamfunction at the first three orders when the first harmonic is propagating but the second is evanescent, $\omega < N < 2\omega$. The tangent functions are replaced by explicit square roots when the corresponding frequency is above the buoyancy frequency.

motors positioned at a pitch of 10 mm along the flexible section, each of which has a vertical resolution of 0.0127 mm and a stroke of 48 mm.

For generating the digital input signals to these stepper motors, we constructed a coupled set of Texas Instruments Beaglebone Blacks (revision C). Each Beaglebone contains a processor where every instruction takes exactly 5 ns, on which we deploy an efficient assembly-language algorithm to issue signals to motor drivers. The signal timings are compiled from analytic functions specified in a text file. The waveforms produced for this paper have a temporal resolution of 30 ns.

The surface of the wave maker is a 3 mm-thick nylon-faced neoprene foam sheet (similar to that used for wetsuits). At zero displacement, the neoprene surface is flush with the base of the tank, but in operation is deformed by 100 horizontal rods, each spanning the width of the tank and driven by one of the stepper motors. The lengthwise edges of the sheet are not sealed to the tank wall, and there is an 80 mm-deep cavity of fluid beneath the neoprene with both sides of the sheet wetted. However, there is almost no pressure gradient to drive a leakage flow from the underlying cavity into the working section of the tank, provided the chosen waveform conserves volume. To leading order, three-dimensional effects are limited to wall boundary layers.

The neoprene attaches to sleeves around the horizontal rods using hook-and-loop fasteners. The material has some resistance to bending, and conveniently the sleeves can rotate about the rods, minimising the tensile stress in the sheet and the bending moments on the actuators. Our modelling (Dobra *et al.* 2019) indicates that this produces C^2-continuous profiles, despite being specified by a discrete set of actuation rods. We find that the wave maker can reliably produce sinusoids of steepness $\left|\frac{\partial h}{\partial x}\right| \leqslant 0.6$ without the motors stalling or neoprene detaching.

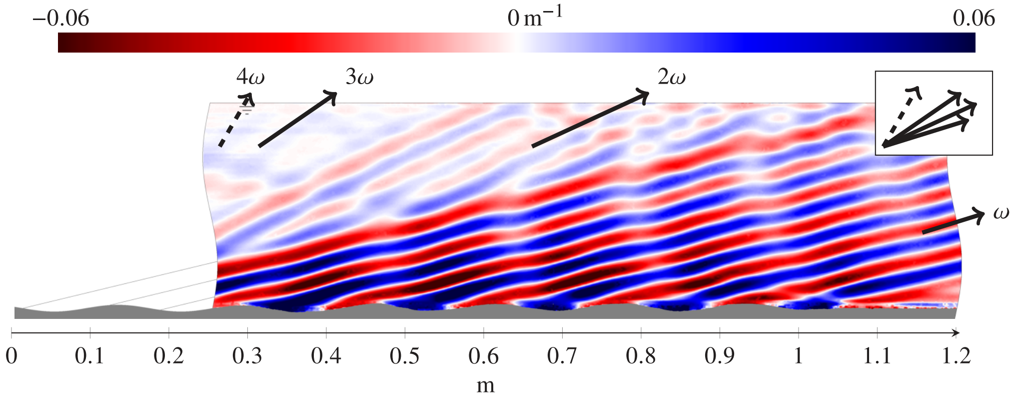

Figure 3: Vertical gradient of the normalised density perturbation, $\frac{1}{\rho_{00}}\frac{\partial \rho'}{\partial z}$, for a sinusoid of input amplitude 4 mm when $\omega = 0.3\,\mathrm{rad\,s^{-1}}$, $k = 40\,\mathrm{rad\,m^{-1}}$ and $N = 1.58\,\mathrm{rad\,s^{-1}}$, exhibiting four harmonics, indicated by the arrows. The fourth harmonic is just visible but is too weak to measure its amplitude using our diagnostics.

4.2. *Method*

We filled the tank using the double bucket method (Fortuin 1960; Oster 1965) with a linear density stratification of the form $\rho_0(z) = \rho_{00} + z\frac{d\rho_0}{dz}$, which gives a constant buoyancy frequency $N = 1.58\,\mathrm{rad\,s^{-1}}$, using sodium chloride as the solute.

Quasi-monochromatic waveforms of six complete wavelengths $\left(k = 40\,\mathrm{rad\,m^{-1}}\right)$ were driven along the magic carpet. Starting from rest, we increased the amplitude at a constant rate of $2\,\mathrm{mm\,min^{-1}}$ until the desired amplitude was obtained. By increasing the amplitude slowly, the formation of a boundary layer was minimised, ensuring maximum transmission of internal waves. Then, the wave maker continued to run at constant amplitude for 80 s for data acquisition, before decreasing the amplitude at a rate of $6\,\mathrm{mm\,min^{-1}}$ in order to minimise mixing in the tank due to impulsive flows, which would degrade the stratification for future runs. A typical wave field is shown in figure 3.

We observed the produced density perturbations using the optical technique of Synthetic Schlieren (Dalziel *et al.* 1998; Sutherland *et al.* 1999; Dalziel *et al.* 2000). A static, random pattern of black and white dots was displayed 0.2 m behind the tank on a 1.4 m (55″) diagonal size 4k (UHD) television screen, in order to maximise the contrast between colours, similar to that implemented by Sveen & Dalziel (2005). The light rays emitted by the screen bend as they pass through the varying refractive indices in the tank, and the distorted image was recorded at 4 fps on a 12-megapixel ISVI IC-X12CXP video camera located 3.8 m in front of the tank. A pattern-matching algorithm in the software package DigiFlow (Dalziel Research Partners 2018) was used to reconstruct the density fields from the recorded images.

To measure the amplitudes of the harmonics produced, we cropped the output video sequence from the Synthetic Schlieren to a rectangular window, entirely contained in all of the observed wave beams, that was 0.32 m wide and 0.11 m high and its base was 0.034 m above the surface of the wave maker. By excluding the region very close to the wave maker, any boundary layer effects are eliminated from this analysis. Within this window, we used harmonic analysis to extract the amplitude and phase of each of the harmonics. Any real signal $f(t)$ that is periodic with period $2T$ can be expressed as the complex Fourier series,

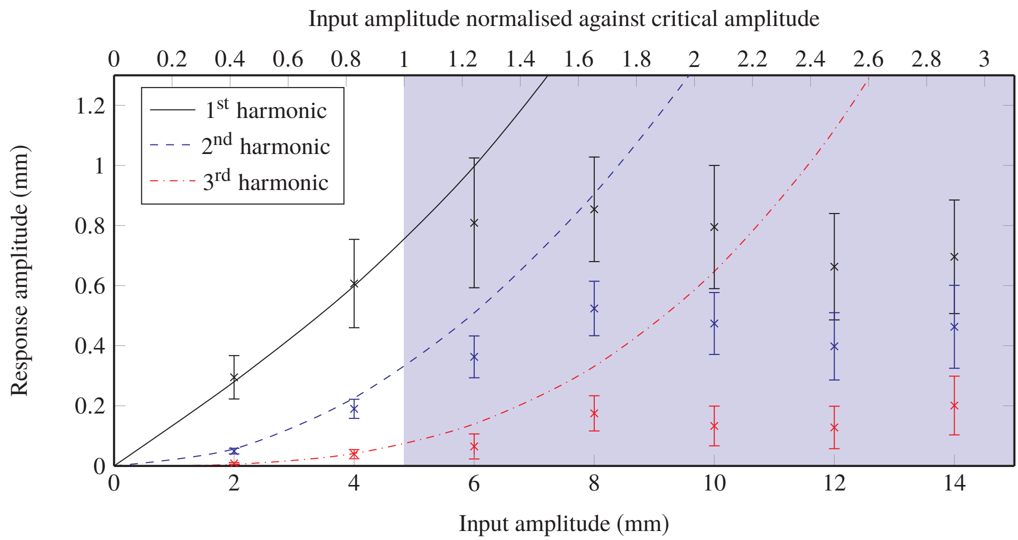

Figure 4: Observed vertical displacement amplitudes of the first three harmonics (points with error bars) compared to predictions correct to third order (lines) for monochromatic sinusoids with frequency $0.3\,\mathrm{rad\,s^{-1}}$. The predictions are linearly scaled by a factor of 0.14 to match the smaller responses generated by the wave maker. A fourth harmonic was observed but is too weak to be analysed.

using an asterisk * to denote the complex conjugate,

$$f(t) = c_0 + \sum_{n=1}^{\infty}\left[c_n \mathrm{e}^{\mathrm{i}\frac{n\pi t}{T}} + c_n^* \mathrm{e}^{-\mathrm{i}\frac{n\pi t}{T}}\right], \tag{4.1}$$

with the complex coefficients given by

$$c_n = \frac{1}{2pT}\int_0^{2pT} f(t)\mathrm{e}^{-\mathrm{i}\frac{n\pi t}{T}}\,\mathrm{d}t, \tag{4.2}$$

averaged over p complete periods to reduce experimental noise. The choice of summing only over positive n is possible because the function $f(t)$ being real requires $c_{-n} = c_n^*$. Each pixel in an image sequence is treated as an independent signal, $f_j(t)$, and its first few Fourier coefficients, c_n, are found. The amplitude of the signal with angular frequency $\omega = \frac{n\pi}{T}$ is given by $\frac{|c_n|}{2}$ and phase by the argument of c_n. Then, the pixels are assembled to form amplitude and phase images at each harmonic frequency.

For each mode, the dominant internal wave travels up and to the right (with a very weak wave to the left, as observed by Mercier *et al.* (2010)) before reflecting off the top surface of the water to travel down and to the right. To separate these and provide the amplitude of the dominant wave at each pixel, we applied the Hilbert transform to each mode, which filters by direction in wavevector space and was first applied to internal waves by Mercier *et al.* (2008). Finally, we estimated the amplitude of each harmonic by taking the mean over all points in the window and also calculated the standard deviation to evaluate the uncertainty.

4.3. *Results and discussion*

Graphs comparing the measured amplitudes of each of the harmonics against the theoretical predictions in table 2 are shown in figure 4 for input frequency $\omega = 0.3\,\mathrm{rad\,s^{-1}} = 0.190N$

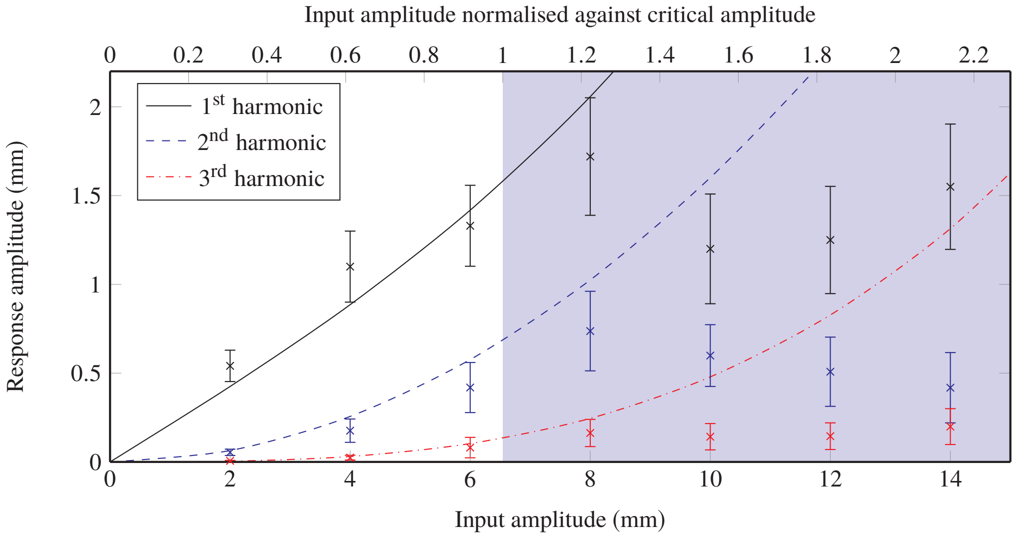

Figure 5: Observed vertical displacement amplitudes of the first three harmonics (points with error bars) compared to predictions correct to third order (lines) for monochromatic sinusoids with frequency 0.4 rad s^{-1}. The predictions are linearly scaled by a factor of 0.21.

and in figure 5 for $\omega = 0.4\,\mathrm{rad\,s^{-1}} = 0.253N$. The error bars represent one standard deviation either side of the mean of the measured amplitude after taking the Hilbert transform (see §4.2). The first four harmonics are propagating waves in the first set, but only the first three are propagating in the second set. However, the signal-to-noise ratio using our apparatus for the fourth harmonic is very low, so we cannot reliably measure its very small amplitude of order 0.01 mm, in the domain of validity, and we omit it from figure 4.

From these graphs, we find that our solution predicts the relative amplitudes of the harmonics well at moderately low amplitudes, within the weakly nonlinear regime. In particular, we observe the predicted superlinear growth of the first harmonic. As stated in §3.1, our model assumes that each internal wave characteristic only intersects the wave maker once. This requires the gradient of the fundamental mode, $\cot\Theta_1$, to be greater than the maximum gradient of the input sinusoid, $a = Ak$. Thus, the domain of applicability is $A < \frac{1}{k}\cot\Theta_1$, which is the unshaded region on the graphs, and we do not expect the experimental data to fit the predictions in the shaded regions. Nevertheless, the experiments still conform fairly well to the theory just above this critical amplitude.

We needed to linearly scale down all of the predictions in order to match the experiments. The scaling factor is uniform for each graph, that is for each input frequency, wavelength and buoyancy frequency but it is independent of the amplitude. This factor is a measure of the efficiency of our "magic carpet" at generating internal waves: no scaling would be required if the vertical displacement of the fluid equals the vertical displacement of the wave maker. It arises because of the formation of a boundary layer in the vicinity of the wave maker, where the flow ceases to follow the strict characteristic structure of linear internal waves. Instead, the material surface at the top edge of the boundary layer is deformed by the complex flow beneath, and the laminar internal waves are effectively generated by this oscillating surface. This boundary layer also forms around oscillating bodies within the stratification (Ermanyuk 2000; Clark & Sutherland 2010) and near cam-driven wave generators (Gostiaux *et al.* 2007; Mercier *et al.* 2010), which exhibit displacement efficiencies of around 0.5 in near-optimal cases. Displacement efficiency of our wave maker is a propagation-angle-dependent quantity, which ranges from 0.1 to 0.9 (Dobra 2018). In the present experiments where fundamentals emanate obliquely, these are 0.14 (figure 4) and 0.21 (figure 5).

In addition, the stratification within the boundary layer is not uniform. Firstly, moving the boundary into the stratification is likely to cause enhanced diffusion due to the deformation of isopycnals and possibly small-scale turbulent mixing. Secondly, although assumed to the contrary, salt is perpetually diffusing through the tank at a rate proportional to the saline gradient. However, salt cannot diffuse through the base of the tank, so the density gradient and hence the buoyancy frequency are zero there. Thus, there is an unknown stratification within the boundary layer. Consequently, our model should only be applied to the material surface at the top of the boundary layer.

Above the critical amplitude, there is a regime change: the response amplitudes of the harmonics cease growing and the higher frequencies contain a greater proportion of the energy. Here, shear flows within the boundary layer generate turbulence and significant flow separation occurs. As a result, a broader frequency and wavevector spectrum is generated at values ceasing to be restricted to integer multiples of the input waveform. Therefore, increasing amounts of energy are dispersed into frequencies not measured here and our weakly nonlinear model is thoroughly violated at large amplitudes.

5. Generating a pure wavefield

5.1. *Approach*

We saw in §3.4 that a monochromatic boundary forcing produces a full spectrum of internal wave harmonics. However, to study the free-space dynamics of internal waves experimentally, such as for the interaction of two incident wave beams (Smith & Crockett 2014), wave fields without the extra harmonics are desirable.

One approach is to modify the wave maker so that it is mounted perpendicular to the characteristics of the intended internal wave, thus at angle Θ to the horizontal. Then, the velocity of the surface of the modified wave maker, $\mathbf{U}$, is always perpendicular to its equilibrium plane, thus has the same direction as the characteristics of the internal wave and hence the fluid velocity, $\mathbf{u}$. Therefore, the kinematic boundary condition (2.15) implies that $\mathbf{U} = \mathbf{u}$ on the wave maker surface, and the monochromatic response exactly satisfies the nonlinear boundary condition, so no additional harmonics are generated. Moreover, a monochromatic sinusoidal internal wave of any amplitude satisfies the linear internal wave equation (3.3) (McEwan 1973), so the response is monochromatic even in the strongly nonlinear regime, provided there is no overturning or shear instability. In particular, we note that for our unmodified horizontal wave maker, critically evanescent internal waves ($\omega = N$) have vertical characteristics, which are perpendicular to our wave maker, so these are the only monochromatic fluid oscillations for which our horizontal wave maker can eliminate harmonics entirely.

Alternatively, we can use the unique ability of our wave maker to choose a polychromatic input waveform that generates a monochromatic wave at some other angle to the vertical, Θ. As an example, suppose we wish to solve the inverse problem of constructing the input waveform, h, that produces exactly the internal wave field (3.20) of the linear solution in §3.2, then we would have

$$\psi = a\hat{\psi} = -\frac{a\omega}{k^2}\sin\left[k(x - z\tan\Theta) - \omega t\right]. \tag{5.1}$$

We know from §3 that the wave maker profile

$$h = ah_1 = A\sin(kx - \omega t) = \frac{a}{k}\sin\phi \tag{5.2}$$

is the leading-order (linear) input required to generate ψ, but it also produces higher harmonics that are in this case unwanted. Thus, seeking a solution valid in the weakly nonlinear regime ($|a| \ll 1$), this time we expand h and seek a series solution of the form,

$$h = \sum_{n=1}^{\infty} a^n h_n, \tag{5.3}$$

that generates the monochromatic internal wave field (5.1).

At $\mathrm{ord}(a^2)$, the second harmonic that is generated by the linear forcing (5.2) is given by ψ_2, which is stated in table 2. We can cancel this second harmonic by superposing a corresponding correction, $a^2 h_2$, on the wave maker. Since the linearised kinematic boundary condition (3.4) is $\frac{\partial h}{\partial t} = \left.\frac{\partial \psi}{\partial x}\right|_{z=0}$ and it needs to negate ψ_2, we deduce that

$$h_2 = -\int \left.\frac{\partial \psi_2}{\partial x}\right|_{z=0} \mathrm{d}t = -\frac{1}{2k}\tan\Theta \sin[2(kx - \omega t)], \tag{5.4}$$

with the constant of integration set to zero so that $\langle h \rangle = 0$. It then follows that

$$h = \frac{a}{k}\sin\phi - \frac{a^2}{2k}\tan\Theta\sin(2\phi) + O\left(a^3\right). \tag{5.5}$$

However, since the input waveform has now been modified, $h \neq A\sin\phi$, the expansion of the kinematic boundary condition (2.16) needs to be recalculated to obtain the internal wave field at $\mathrm{ord}(a^3)$, ψ_3, which would then lead to further such corrections.

5.2. *Kinematic boundary condition*

Such approaches rapidly become unwieldy. Instead, we take the approach that our wave field is entirely specified by $\psi = a\hat{\psi}$ and by this definition one cannot make higher order corrections to ψ. Instead, we choose to expand the dependent function, h, using (5.3) in the Taylor-expanded kinematic boundary condition (2.17),

$$\sum_{q=0}^{\infty} \frac{h^q}{q!}\left(\frac{\partial}{\partial x} + \frac{\partial h}{\partial x}\frac{\partial}{\partial z}\right)\left.\frac{\partial^q \psi}{\partial z^q}\right|_{z=0} = \frac{\partial h}{\partial t}, \tag{5.6}$$

which gives

$$\sum_{q=0}^{\infty} \frac{1}{q!}\left(\sum_{s=1}^{\infty} a^s h_s\right)^q \left(\frac{\partial}{\partial x} + \left(\sum_{r=1}^{\infty} a^r \frac{\partial h_r}{\partial x}\right)\frac{\partial}{\partial z}\right)\left.\frac{\partial^q (a\hat{\psi})}{\partial z^q}\right|_{z=0} = \sum_{n=1}^{\infty} a^n \frac{\partial h_n}{\partial t}. \tag{5.7}$$

Although a truncation of this expansion of h may generate evanescent harmonics, this possibility does not need to be considered here, because the only fluid flows are those specified in $\hat{\psi}$, which can consist of arbitrary non-internal wave motions.

Next, we manipulate this expansion to factor out all the powers of a. Firstly, we re-express the infinite sum raised to an arbitrary finite integer q as a new power series,

$$\left(\sum_{s=1}^{\infty} a^s h_s\right)^q = a^q\left(\sum_{s=0}^{\infty} a^s h_{s+1}\right)^q = a^q \sum_{s=0}^{\infty} a^s c_s, \tag{5.8}$$

where the coefficients c_s are given by the recurrence relation,

$$c_{s+1}(q) = \frac{1}{(s+1)h_1} \sum_{p=0}^{s} [q(s+1) - p(q+1)] c_p h_{s-p+2}, \tag{5.9}$$

and $c_0 = h_1^q$. While aspects of this formula are standard material (see, for example, Gradshteyn & Ryzhik 2014), appendix B contains our derivation, from which we obtain the next three coefficients,

$$c_1 = q h_1^{q-1} h_2, \tag{5.10a}$$

$$c_2 = \frac{1}{2h_1}[2q h_3 c_0 + (q-1) h_2 c_1] = q h_1^{q-1} h_3 + \frac{1}{2} q(q-1) h_1^{q-2} h_2^2, \tag{5.10b}$$

$$\begin{aligned} c_3 &= \frac{1}{3h_1}[3q h_4 c_0 + (2q-1) h_3 c_1 + (q-2) h_2 c_2] \\ &= q h_1^{q-1} h_4 + q(q-1) h_1^{q-2} h_2 h_3 + \frac{1}{6} q(q-1)(q-2) h_1^{q-3} h_2^3. \end{aligned} \tag{5.10c}$$

Then, the kinematic boundary condition becomes

$$\sum_{q=0}^{\infty} \frac{a^{q+1}}{q!} \left(\sum_{s=0}^{\infty} a^s c_s(q) \right) \left(\left. \frac{\partial^{q+1} \hat{\psi}}{\partial x\, \partial z^q} \right|_{z=0} + \left. \frac{\partial^{q+1} \hat{\psi}}{\partial z^{q+1}} \right|_{z=0} \sum_{r=1}^{\infty} a^r \frac{\partial h_r}{\partial x} \right) = \sum_{n=1}^{\infty} a^n \frac{\partial h_n}{\partial t}. \tag{5.11}$$

The first term can be straightforwardly rearranged to isolate powers of a. The second term requires the Cauchy product (B 5), which evaluates the product of two summations, before the reorganisation in powers of a,

$$\sum_{q=0}^{\infty} \sum_{s=0}^{\infty} \frac{a^{q+s+1}}{q!} \left(c_s(q) \left. \frac{\partial^{q+1} \hat{\psi}}{\partial x\, \partial z^q} \right|_{z=0} + \left. \frac{\partial^{q+1} \hat{\psi}}{\partial z^{q+1}} \right|_{z=0} \sum_{r=1}^{s} c_{s-r}(q) \frac{\partial h_r}{\partial x} \right) = \sum_{n=1}^{\infty} a^n \frac{\partial h_n}{\partial t}. \tag{5.12}$$

Finally, letting $n = q + s + 1$ and adjusting the summation limits accordingly gives the expansion of the kinematic boundary condition factorised into powers of a,

$$\sum_{n=1}^{\infty} \sum_{q=0}^{n-1} \frac{a^n}{q!} \left(c_{n-q-1}(q) \left. \frac{\partial^{q+1} \hat{\psi}}{\partial x\, \partial z^q} \right|_{z=0} + \left. \frac{\partial^{q+1} \hat{\psi}}{\partial z^{q+1}} \right|_{z=0} \sum_{r=1}^{n-q-1} c_{n-q-r-1}(q) \frac{\partial h_r}{\partial x} \right) = \sum_{n=1}^{\infty} a^n \frac{\partial h_n}{\partial t}. \tag{5.13}$$

In this structure, at ord(a^n), h_n only appears on the right hand side. On the left hand side, the c_s terms produce orders of h up to $s+1$, but $c_0(0) = 1$ and $c_s(0) = 0$ for $s \geqslant 1$, so the highest order appearing is h_{n-1}. Thus, h_n depends only on lower order contributions to the solution, and we obtain a similar hierarchy of dependencies to that found for ψ_n in §2.2 (depicted in figure 1).

This boundary condition (5.13) holds for any fluid flow, $\hat{\psi}$, in the weakly nonlinear regime, which need not consist of internal waves. Since it is derived only from the kinematic boundary condition (2.15) of no penetration and thus is only evaluated at the boundary, this equation is independent of the fluid dynamics in the interior of the domain, provided the flow is inviscid and incompressible, and holds for arbitrary density stratifications, or indeed no stratification at all. As a result, not only can we prescribe the wave maker displacement, $h(x,t)$, required for any arbitrary flow field, but we can also solve the inverse problem of deducing a suitable displacement on the wave maker that will fully absorb any incoming waves: a non-reflecting boundary condition for internal waves. Furthermore, given sufficiently many spatially separate measurements of velocity distant from $z = 0$, the Taylor's expansion at $z = 0$ can be computed and thus the spectrum of the source may be inferred.

Result: h

$h \leftarrow 0$
for $n \in \mathbb{N}$ **do**
  Evaluate kinematic boundary condition (5.13) at ord(a^n)
  Calculate $c_{n-1}(q; h_1, \ldots, h_{n-1})$ using (5.9)
  Calculate $\left.\frac{\partial^n \hat{\psi}}{\partial x \partial z^{n-1}}\right|_{z=0}$, $\left.\frac{\partial^{n-1} \hat{\psi}}{\partial z^{n-1}}\right|_{z=0}$ and $\frac{\partial h_{n-1}}{\partial x}$ following the pattern of (5.15*b*)
  Substitute these calculated quantities into (5.13) at ord(a^n)
  Express the terms as products of $\sin\phi$ and $\cos\phi$ using (3.33)
  Express the trigonometric products as sums of harmonics using ALGORITHM 2
  Integrate with respect to t, setting the integration constant to zero
  $h \leftarrow h + a^n h_n$
end

ALGORITHM 3. Calculation of boundary displacement, h, to obtain a single set of internal wave harmonics with a common phase angle.

5.3. *Algorithmic calculation of boundary displacement for a single spectrum of internal wave harmonics*

We consider a single spectrum of harmonics to be one arising from a common fundamental, so have frequencies $n\omega$ that are integer multiples of the fundamental and have a common horizontal phase velocity, c_x, which restricts the wavevectors to be $\mathbf{k}_n = (nk, -nk\tan\Theta_n)$. This is sufficiently general to admit a polychromatic spectrum constructed with arbitrary amplitudes of such harmonics to form a Fourier series and thus may represent arbitrary translating periodic shapes. In this section, we present a procedure to explicitly calculate order-by-order the boundary displacement, h, required to generate a single spectrum of internal wave harmonics with streamfunction $\psi = a\hat{\psi}$; this is summarised in algorithm 3. As an example, we illustrate how a polychromatic spectrum of three harmonics would be expanded to obtain h correct to second order, with related expressions listed in tables 4 and 5. We then specialise to a monochromatic wave and give the corresponding boundary displacement in table 6.

To calculate h_n, first we take all of the terms at ord(a^n) in the kinematic boundary condition (5.13). We note that the linear condition is the same as for the forwards problem (3.4). Second, we evaluate the coefficients c_s in terms of h_q and substitute these into the boundary condition; these are listed for the first three orders in table 4. Third, we evaluate and substitute all of the required derivatives and boundary displacement contributions. The expansion is now a sum of products of sines and cosines with phases of the form $\alpha\phi$, where $\alpha \in \mathbb{Z}$. Exactly as in §3.4, we re-express these as a sum of terms of the form $\sin^\alpha\phi\cos^\beta\phi$, where $\alpha, \beta \in \mathbb{Z}$, using the general compound angle formulae (3.33), and then convert them to a sum of harmonics using algorithm 2 (see appendix A for derivations of these formulae). After simplification, we are left with $\frac{\partial h_n}{\partial t}$ equal to a sum of harmonics with fundamental phase ϕ. We integrate this with respect to time, t, setting the integration constant to zero to enforce no net displacement. This yields the contribution to h at n^{th} order.

For example, the contributions to the boundary displacement correct to second order, $h = ah_1 + a^2 h_2$, for a polychromatic internal wave field consisting of three harmonics that are in phase at $z = 0$,

$$\begin{aligned}\psi = a\hat{\psi} = A_1 \sin[k(x - z\tan\Theta_1) - \omega t] + A_2 \sin[2k(x - z\tan\Theta_2) - 2\omega t] \\ + A_3 \sin[3k(x - z\tan\Theta_3) - 3\omega t],\end{aligned} \tag{5.14}$$

are listed in table 5. In line with §3, we define a to be the characteristic steepness of the first

Order	Kinematic boundary condition at n^{th} order
1^{st}	$\left.\dfrac{\partial\hat{\psi}}{\partial x}\right\|_{z=0} = \dfrac{\partial h_1}{\partial t}$
2^{nd}	$\left.\dfrac{\partial\hat{\psi}}{\partial z}\right\|_{z=0} + h_1 \left.\dfrac{\partial^2\hat{\psi}}{\partial x\,\partial z}\right\|_{z=0} = \dfrac{\partial h_2}{\partial t}$
3^{rd}	$\dfrac{\partial h_2}{\partial x}\left.\dfrac{\partial\hat{\psi}}{\partial z}\right\|_{z=0} + h_2 \left.\dfrac{\partial^2\hat{\psi}}{\partial x\,\partial z}\right\|_{z=0} + h_1 \dfrac{\partial h_1}{\partial x}\left.\dfrac{\partial^2\hat{\psi}}{\partial z^2}\right\|_{z=0} + \dfrac{1}{2}h_1^2 \left.\dfrac{\partial^3\hat{\psi}}{\partial x\,\partial z^2}\right\|_{z=0} = \dfrac{\partial h_3}{\partial t}$

Table 4: Kinematic boundary condition at the first three orders, after the c_s coefficients have been expanded in terms of h_q.

Order	Contribution to the boundary displacement, h_n
1^{st}	$-\dfrac{1}{k}\sin\phi - \dfrac{A_2}{kA_1}\sin(2\phi) - \dfrac{A_3}{kA_1}\sin(3\phi)$
2^{nd}	$-\dfrac{A_2}{2kA_1}\left[\tan\Theta_1 - 2\tan\Theta_2 + \dfrac{A_3}{A_1}(2\tan\Theta_2 - 3\tan\Theta_3)\right]\sin\phi$ $-\dfrac{1}{2k}\left[\tan\Theta_1 + \dfrac{A_3}{A_1}(\tan\Theta_1 - 3\tan\Theta_2)\right]\sin(2\phi)$ $-\dfrac{A_2}{2kA_1}[\tan\Theta_1 + 2\tan\Theta_2]\sin(3\phi) - \dfrac{A_2A_3}{2kA_1^2}[2\tan\Theta_2 + 3\tan\Theta_3]\sin(5\phi)$

Table 5: Contributions to the boundary displacement at the first two orders that generates three in-phase internal wave harmonics (5.14).

harmonic of h predicted by linear theory, $a = \frac{A_1k^2}{\omega}$. Expanding to third order would introduce up to five harmonics along the boundary, but if expanded to all orders, these components would cancel to produce only three internal wave harmonics.

Specialising further to generate a monochromatic internal wave field (5.1) with $A_1 = -\frac{a\omega}{k^2}$ and $A_2 = A_3 = 0$, we note that $\frac{\partial}{\partial z} = -\tan\Theta\frac{\partial}{\partial x}$ due to the characteristic structure, so the kinematic boundary condition (5.13) specialises to

$$\sum_{n=1}^{\infty}\sum_{q=0}^{n-1}\frac{a^n}{q!}\left.\frac{\partial^{q+1}\hat{\psi}}{\partial x\,\partial z^q}\right|_{z=0}\left(c_{n-q-1} - \tan\Theta\sum_{r=1}^{n-q-1}c_{n-q-r-1}\frac{\partial h_r}{\partial x}\right) = \sum_{n=1}^{\infty}a^n\frac{\partial h_n}{\partial t}. \tag{5.15a}$$

Recalling that $\phi = kx - \omega t$, the derivatives of the streamfunction, following formula (3.32a), are given by

$$\left.\frac{\partial^{q+1}\hat{\psi}}{\partial x\,\partial z^q}\right|_{z=0} = \begin{cases}(-1)^{\frac{q+2}{2}}\omega k^{q-1}\tan^q\Theta\cos\phi & \text{for even } q\\ (-1)^{\frac{q+1}{2}}\omega k^{q-1}\tan^q\Theta\sin\phi & \text{for odd } q\end{cases}. \tag{5.15b}$$

The contributions to the boundary displacement at the first three orders that generate a monochromatic internal wave are listed in table 6. The first two orders agree with the

Order	Contribution to the boundary displacement, h_n
1^{st}	$\dfrac{1}{k}\sin\phi$
2^{nd}	$-\dfrac{1}{2k}\tan\Theta\sin(2\phi)$
3^{rd}	$\dfrac{1}{k}\tan^2\Theta\left\{\dfrac{3}{8}\sin(3\phi)-\dfrac{1}{8}\sin\phi\right\}$

Table 6: Contributions to the boundary displacement at the first three orders that generates a monochromatic internal wave (5.1).

solution for h (5.5) inferred from the internal wave field generated by a monochromatic boundary forcing in §5.1. As we would expect from the forwards problem at third order, a third harmonic is required on the boundary to eliminate the third harmonic internal wave that would be generated by a monochromatic boundary displacement. However, this is not simply the negative of the third-order wave field, ψ_3 (as listed in table 2), generated by a monochromatic forcing along the boundary. Nonetheless, it does exhibit a third-order reduction that is cubic in a to the amplitude fundamental frequency along the wave maker. This qualitatively agrees with the observation in §3.4 that there is a cubically increasing response in the fundamental frequency internal wave due to a monochromatic forcing, so we expect a cubically decreasing input to counteract this and generate an internal wave field of a given amplitude.

We remark that we could have alternatively derived the expanded kinematic boundary condition for a monochromatic internal wave (5.15) by directly considering the fluid velocities projected onto the direction of motion of the wave maker. Doing so for arbitrarily large amplitudes produces physical inconsistencies, because our wave maker cannot take multiple values of h at any value of x. However, within the single-valued constraint, it is possible to compute an $h(x, t)$ that matches a wave of arbitrary amplitude. One obtains a strongly nonlinear equation where the dependent variable appears both inside and outside a trigonometric function. This can be resolved by Taylor expanding on those trigonometric functions and this leads to an expansion in h that is identical to equation (5.15). The details of this calculation can be found in appendix C.

5.4. *Experimental verification*

We experimentally tested the predictions for a single spectrum of harmonics in §5.3 using the apparatus and method described in §4.1–4.2. For these experiments, the tank contained a nearly linear stratification of buoyancy frequency $N = 1.4\,\mathrm{rad\,s^{-1}}$.

Initially, we displaced the magic carpet with a right-travelling monochromatic sinusoid of frequency $\omega = 0.3\,\mathrm{rad\,s^{-1}} = 0.21N$, wavenumber $k = 40\,\mathrm{rad\,m^{-1}}$ and steady amplitude $A = 4\,\mathrm{mm}$, giving $Ak = 0.16$; the resulting wave field is shown in figure 6(*a*). As expected from §3, there is a dominant first harmonic plus a visible second harmonic, but negligible third harmonic. In contrast, we applied the corresponding second-order correction of table 6 in figure 6(*b*) to almost eliminate the second harmonic but consequently generated a significant third harmonic. We were unable to completely remove the second harmonic using our theoretical waveform because of the nonlinear stratification and flow in the boundary layer highlighted in §4.3, which cannot be accommodated in this solution. Nevertheless, we have

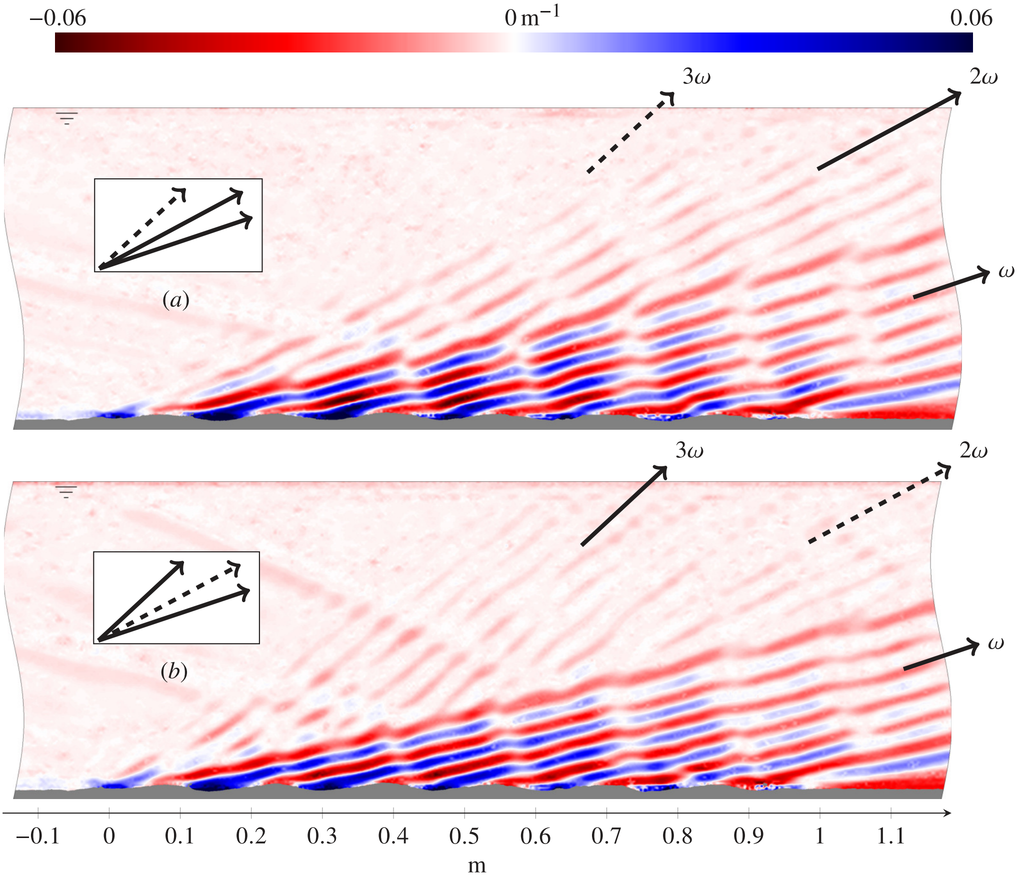

Figure 6: Vertical gradient of the normalised density perturbation $\frac{1}{\rho_{00}}\frac{\partial \rho'}{\partial z}$ for: (*a*) a monochromatic sinusoid of amplitude 4 mm, frequency 0.3 rad s^{-1} and wavenumber 40 rad m^{-1} in a stratification where the harmonic sequence decays in amplitude; and (*b*) the corresponding polychromatic input to remove the second-order contributions to the second harmonic, which in this configuration generates a significant third harmonic, as expected. Harmonic analysis confirms that wavy perturbations in phase lines are not intrinsic to the first harmonic.

demonstrated a useful technique in the experimental study of internal waves: the substantial attenuation of an unwanted harmonic, which allows a clearer view of the desired fundamental wave beam.

To test the polychromatic expansion given in table 5, we estimated the amplitudes of the three internal wave harmonics in figure 6(*b*) using the method in §4.2 and then reconstructed the corresponding theoretical boundary displacement correct to second order. We found that the second and third harmonics were in antiphase relative to the first harmonic, so we multiplied the corresponding amplitudes in the model by −1. Figure 7 compares the inferred displacement, shown with a solid line, with the actual input along the "magic carpet" linearly scaled by a factor of 0.19, shown with a dashed line. A pure sinusoid is also drawn in dots to demonstrate the modulation of a sinusoid introduced by our expansion (5.13). The very similar shapes of the inferred and input waveforms, except at phases corresponding to distance 0 m along the wave maker, confirm that the second-order correction accurately determines the amplitude of the second harmonic relative to the first harmonic. The small

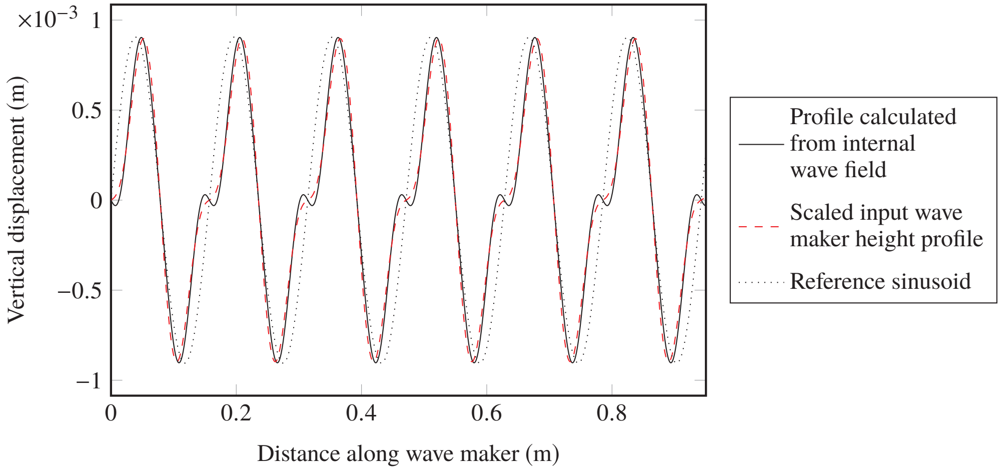

Figure 7: Vertical displacement profile calculated from the experiment in figure 6(*b*) showing a good match to the input waveform, scaled down linearly to match the amplitudes. Also shown, for reference, is a monochromatic sinusoid.

disagreement between the two curves arises principally from an overestimation of the third harmonic. This is partially due to already identified difficulty in measuring the amplitudes of weak harmonics but also due to the boundary layer around the wave maker. The calculated profile is in fact for a material surface just outside the boundary layer. Despite this small error, we have successfully calculated the boundary displacement required to produce an observed spectrum of waves, with a superior accuracy that would be given by a linear model.

6. Conclusion

We demonstrated that triadic wave-wave interactions do not occur between internal waves sharing the same horizontal component of the phase velocity. This has profound implications for the spectral structure in many applications where the wave field is generated by what is essentially a propagating boundary. In particular, the only source of waves, or of their harmonics, is at the boundary itself. Consequently, the wave field encodes considerable information about the boundary geometry. We have derived a complementary pair of weakly nonlinear perturbation expansions: one to predict the spectrum of harmonics of internal waves generated by a prescribed boundary displacement, and its inverse to calculate the boundary displacement required to produce a given flow field. Both of these expansions were specialised to a monochromatic boundary displacement and a monochromatic internal wave field, respectively, for which we gave succinct algorithms for calculating the corresponding polychromatic spectra. Each successive order of the expansions not only introduces an additional harmonic but also applies additive corrections to the lower harmonics. We successfully verified our models using experiments driven by a “magic carpet” in the base of a large tank. Our results may be used to generate cleaner internal wave fields, especially monochromatic ones, in the laboratory, and to deduce the boundary displacements corresponding to an observed flow field, whether in a tank or in the ocean.

Appendix A. Compound angle identities

The formulae in this appendix are used for algorithmically evaluating the perturbation expansions of this paper at all orders.

A.1. *Product of sinusoids as a sum of harmonics*

The expansions throughout this paper frequently yield products of cosines and sines that we need to express as a sum of harmonics. We consider the arbitrary product for a single phase ϕ expressed as complex exponentials, for $\alpha, \beta \in \mathbb{Z}_{\geqslant 0}$,

$$\cos^{\alpha}\phi\,\sin^{\beta}\phi = \frac{1}{2^{\alpha}}\left(\mathrm{e}^{\mathrm{i}\phi} + \mathrm{e}^{-\mathrm{i}\phi}\right)^{\alpha}\frac{1}{(2\mathrm{i})^{\beta}}\left(\mathrm{e}^{\mathrm{i}\phi} - \mathrm{e}^{-\mathrm{i}\phi}\right)^{\beta}. \tag{A 1}$$

The binomial expansion gives the product of summations, where $\binom{n}{r} = \frac{n!}{r!(n-r)!}$ is the binomial coefficient,

$$\cos^{\alpha}\phi\,\sin^{\beta}\phi = \frac{1}{2^{\alpha+\beta}\mathrm{i}^{\beta}}\left(\sum_{\xi=0}^{\alpha}\binom{\alpha}{\xi}\mathrm{e}^{\mathrm{i}(\alpha-\xi)\phi}\mathrm{e}^{-\mathrm{i}\xi\phi}\right)\left(\sum_{\epsilon=0}^{\beta}\binom{\beta}{\epsilon}\mathrm{e}^{\mathrm{i}(\beta-\epsilon)\phi}(-1)^{\epsilon}\mathrm{e}^{-\mathrm{i}\epsilon\phi}\right), \tag{A 2}$$

which we combine as a double sum,

$$\cos^{\alpha}\phi\,\sin^{\beta}\phi = \frac{1}{2^{\alpha+\beta}\mathrm{i}^{\beta}}\sum_{\xi=0}^{\alpha}\sum_{\epsilon=0}^{\beta}(-1)^{\epsilon}\binom{\alpha}{\xi}\binom{\beta}{\epsilon}\mathrm{e}^{\mathrm{i}(\alpha+\beta-2\xi-2\epsilon)\phi}. \tag{A 3}$$

This summation exhibits symmetry, whereby pairs of terms have the same values of the binomial coefficients, so we can halve the number of terms in the summation. The summation domain is rectangular in (ξ, ϵ) space, and the conjugate pairs of terms are reflections in the line $\xi+\epsilon = \frac{1}{2}(\alpha+\beta)$, shown in red in figure 8, which passes through the centre of the domain. Thus, we split the domain of summation about this line into the shaded and unshaded regions in the figure, neither of which include the symmetry line, and a separate summation over points lying on the line of symmetry itself, which occurs when, and only when, α and β are either both odd or both even,

$$\cos^{\alpha}\phi\,\sin^{\beta}\phi = S_{\text{shaded}} + S_{\text{unshaded}} + S_{\text{line}}. \tag{A 4}$$

In the first (shaded) sum, ξ runs from zero to the lesser of the intersection of the symmetry line with the ϵ axis (exclusive) and the right edge of the rectangle ($\xi = \alpha$, inclusive), and ξ runs from zero to the lesser of the symmetry line (exclusive) and the top edge of the rectangle ($\epsilon = \beta$, inclusive),

$$S_{\text{shaded}} = \frac{1}{2^{\alpha+\beta}\mathrm{i}^{\beta}}\sum_{\xi=0}^{\left\lfloor\min\left\{\frac{1}{2}(\alpha+\beta-1),\alpha\right\}\right\rfloor}\ \sum_{\epsilon=0}^{\left\lfloor\min\left\{\frac{1}{2}(\alpha+\beta-1)-\xi,\beta\right\}\right\rfloor}(-1)^{\epsilon}\binom{\alpha}{\xi}\binom{\beta}{\epsilon}\mathrm{e}^{\mathrm{i}(\alpha+\beta-2\xi-2\epsilon)\phi}. \tag{A 5}$$

In S_{unshaded}, ξ runs from the greater of the intersection symmetry line with the top edge of the rectangle, $\xi = \frac{1}{2}(\alpha+\beta) - \beta = \frac{1}{2}(\alpha-\beta)$ (exclusive), and the left edge ($\xi = 0$, inclusive) to the right edge ($\xi = \alpha$, inclusive), and ϵ runs from the line of symmetry (exclusive) to the top edge (inclusive),

$$S_{\text{unshaded}} = \frac{1}{2^{\alpha+\beta}\mathrm{i}^{\beta}}\sum_{\xi=\left\lceil\max\left\{\frac{1}{2}(\alpha-\beta+1),0\right\}\right\rceil}^{\alpha}\ \sum_{\epsilon=\left\lceil\max\left\{\frac{1}{2}(\alpha+\beta+1)-\xi,0\right\}\right\rceil}^{\beta}(-1)^{\epsilon}\binom{\alpha}{\xi}\binom{\beta}{\epsilon}\mathrm{e}^{\mathrm{i}(\alpha+\beta-2\xi-2\epsilon)\phi}. \tag{A 6}$$

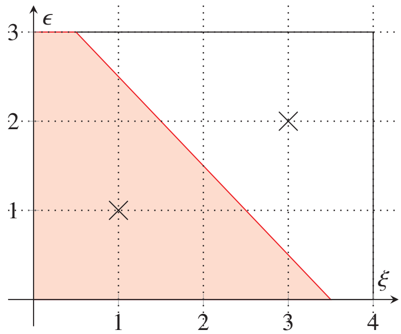

Figure 8: Summation domain for $\cos^4\phi\,\sin^3\phi$ ($\alpha = 4, \beta = 3$). An example pair of conjugate symmetric points is marked with crosses.

We now select a new set of variables to exploit the symmetries, $\mu = \alpha - \xi$ and $\nu = \beta - \epsilon$. On substitution, the summation domains become

$$\left\lceil \max\left\{\frac{1}{2}(\alpha - \beta + 1), 0\right\}\right\rceil \leqslant \alpha - \mu \leqslant \alpha, \tag{A 7a}$$

$$\left\lceil \max\left\{\frac{1}{2}(\alpha + \beta + 1) - (\alpha - \mu), 0\right\}\right\rceil \leqslant \beta - \nu \leqslant \beta. \tag{A 7b}$$

Subtracting α and β from each inequality, respectively, and multiplying through by -1, noting that the maximum functions become minimum functions and the inequalities reverse, gives

$$\left\lfloor \min\left\{\frac{1}{2}(\alpha + \beta - 1), \alpha\right\}\right\rfloor \geqslant \mu \geqslant 0 \quad , \quad \left\lfloor \min\left\{\frac{1}{2}(\alpha + \beta - 1) - \mu, \beta\right\}\right\rfloor \geqslant \nu \geqslant 0, \tag{A 7c}$$

which is exactly the summation domain over (ξ, ϵ) in S_{shaded} (A 5). The binomials, $\binom{\alpha}{\xi} = \binom{\alpha}{\alpha-\mu}$ and $\binom{\beta}{\epsilon} = \binom{\beta}{\beta-\nu}$, are symmetric about $\frac{\alpha}{2}$ and $\frac{\beta}{2}$, respectively, so are equal to their original forms, $\binom{\alpha}{\mu}$ and $\binom{\beta}{\nu}$. Thus, S_{unshaded} is of a very similar form to S_{shaded}

$$S_{\text{unshaded}} = \frac{1}{2^{\alpha+\beta}\mathrm{i}^{\beta}} \sum_{\mu=0}^{\lfloor \min\{\frac{1}{2}(\alpha+\beta-1),\alpha\}\rfloor} \sum_{\nu=0}^{\lfloor \min\{\frac{1}{2}(\alpha+\beta-1)-\mu,\beta\}\rfloor} (-1)^{\beta-\nu}\binom{\alpha}{\mu}\binom{\beta}{\nu}\mathrm{e}^{\mathrm{i}(-\alpha-\beta+2\mu+2\nu)\phi}. \tag{A 8}$$

Since $(-1)^{-\nu} = (-1)^{\nu}$ for $\nu \in \mathbb{Z}$, and on changing the summation variables to (ξ, ϵ), the contributions to $\cos^{\alpha}\phi\,\sin^{\beta}\phi$ not on the line of symmetry total

$$S_{\text{shaded}} + S_{\text{unshaded}} = \frac{1}{2^{\alpha+\beta}\mathrm{i}^{\beta}} \sum_{\xi=0}^{\lfloor \min\{\frac{1}{2}(\alpha+\beta-1),\alpha\}\rfloor} \sum_{\epsilon=0}^{\lfloor \min\{\frac{1}{2}(\alpha+\beta-1)-\xi,\beta\}\rfloor} (-1)^{\epsilon}\binom{\alpha}{\xi}\binom{\beta}{\epsilon}\times \left(\mathrm{e}^{\mathrm{i}(\alpha+\beta-2\xi-2\epsilon)\phi} + (-1)^{\beta}\mathrm{e}^{-\mathrm{i}(\alpha+\beta-2\xi-2\epsilon)\phi}\right). \tag{A 9}$$

The term in the square brackets is $2\cos[(\alpha + \beta - 2\xi - 2\epsilon)\phi]$ when β is even and $2\mathrm{i}\sin[(\alpha + \beta - 2\xi - 2\epsilon)\phi]$ when β is odd. Finally, we choose to sum over harmonics by letting $\gamma = \xi + \epsilon$ and summing over (γ, ϵ). We obtain the summation limits for the shaded region from figure 8 by noting that lines of constant γ are parallel to the red line of symmetry, so $0 \leqslant \gamma \leqslant \left\lfloor \frac{1}{2}(\alpha + \beta - 1)\right\rfloor$, and that the minimum value of ϵ on once such line occurs either on the right or bottom edges of the rectangle and the corresponding maximum value is on the left or top edge, $\max\{\gamma-\alpha,0\} \leqslant \epsilon \leqslant \min\{\gamma,\beta\}$. Thus,

$$S_{\text{shaded}} + S_{\text{unshaded}} = \begin{cases} \frac{(-1)^{\frac{\beta}{2}}}{2^{\alpha+\beta-1}} \sum_{\gamma=0}^{\left\lfloor \frac{1}{2}(\alpha+\beta-1)\right\rfloor} \sum_{\epsilon=\max\{\gamma-\alpha,0\}}^{\min\{\gamma,\beta\}} (-1)^{\epsilon} \binom{\alpha}{\gamma-\epsilon}\binom{\beta}{\epsilon} \cos\left[(\alpha+\beta-2\gamma)\phi\right] & \text{for } \beta \text{ even} \\ \frac{(-1)^{\frac{\beta-1}{2}}}{2^{\alpha+\beta-1}} \sum_{\gamma=0}^{\left\lfloor \frac{1}{2}(\alpha+\beta-1)\right\rfloor} \sum_{\epsilon=\max\{\gamma-\alpha,0\}}^{\min\{\gamma,\beta\}} (-1)^{\epsilon} \binom{\alpha}{\gamma-\epsilon}\binom{\beta}{\epsilon} \sin\left[(\alpha+\beta-2\gamma)\phi\right] & \text{for } \beta \text{ odd} \end{cases}. \tag{A 10}$$

Finally, we consider the contribution along the line of symmetry, where $\gamma = \frac{1}{2}(\alpha+\beta)$ and so ϵ has the same limits as before,

$$S_{\text{line}} = \frac{1}{2^{\alpha+\beta} \mathrm{i}^{\beta}} \sum_{\epsilon=\max\left\{\frac{1}{2}(\beta-\alpha),0\right\}}^{\min\left\{\frac{1}{2}(\alpha+\beta),\beta\right\}} (-1)^{\epsilon} \binom{\alpha}{\frac{1}{2}(\alpha+\beta)-\epsilon}\binom{\beta}{\epsilon}. \tag{A 11}$$

Again, this has a symmetry point at $\epsilon = \frac{\beta}{2}$, so we split the summation into three components, $S_{\text{line}} = S_{\text{lower}} + S_{\text{upper}} + S_{\text{point}}$, where

$$S_{\text{lower}} = \frac{1}{2^{\alpha+\beta} \mathrm{i}^{\beta}} \sum_{\epsilon=\max\left\{\frac{1}{2}(\beta-\alpha),0\right\}}^{\frac{\beta-1}{2}} (-1)^{\epsilon} \binom{\alpha}{\frac{1}{2}(\alpha+\beta)-\epsilon}\binom{\beta}{\epsilon}, \tag{A 12a}$$

$$S_{\text{upper}} = \frac{1}{2^{\alpha+\beta} \mathrm{i}^{\beta}} \sum_{\epsilon=\frac{\beta+1}{2}}^{\min\left\{\frac{1}{2}(\alpha+\beta),\beta\right\}} (-1)^{\epsilon} \binom{\alpha}{\frac{1}{2}(\alpha+\beta)-\epsilon}\binom{\beta}{\epsilon}, \quad \text{and} \tag{A 12b}$$

$$S_{\text{point}} = \begin{cases} \frac{1}{2^{\alpha+\beta} \mathrm{i}^{\beta}} (-1)^{\frac{\beta}{2}} \binom{\alpha}{\frac{\alpha}{2}}\binom{\beta}{\frac{\beta}{2}} & \text{for } \beta \text{ even} \\ 0 & \text{for } \beta \text{ odd} \end{cases}. \tag{A 12c}$$

Similar to the method for S_{unshaded}, changing the summation variable of S_{upper} to $\kappa = \beta - \epsilon$, recalculating the limits and manipulating the binomial coefficients gives

$$S_{\text{upper}} = \frac{1}{2^{\alpha+\beta} \mathrm{i}^{\beta}} \sum_{\kappa=\max\left\{\frac{1}{2}(\beta-\alpha),0\right\}}^{\frac{\beta-1}{2}} (-1)^{\beta-\kappa} \binom{\alpha}{\frac{1}{2}(\alpha+\beta)-\kappa}\binom{\beta}{\kappa} = (-1)^{\beta} S_{\text{lower}}, \tag{A 13}$$

because $(-1)^{-\kappa} = (-1)^{\kappa}$. So, for odd β, the components of S_{line} total zero and for even β, and hence even α (otherwise $S_{\text{line}} = 0$),

$$S_{\text{line}} = \frac{1}{2^{\alpha+\beta}} \binom{\alpha}{\frac{\alpha}{2}}\binom{\beta}{\frac{\beta}{2}} + \frac{(-1)^{\frac{\beta}{2}}}{2^{\alpha+\beta-1}} \sum_{\epsilon=\max\left\{\frac{1}{2}(\beta-\alpha),0\right\}}^{\frac{\beta-1}{2}} (-1)^{\epsilon} \binom{\alpha}{\frac{1}{2}(\alpha+\beta)-\epsilon}\binom{\beta}{\epsilon}. \tag{A 14}$$

Therefore, for $\alpha, \beta, \gamma, \epsilon \in \mathbb{Z}$,

$$
\cos^{\alpha}\phi \, \sin^{\beta}\phi =
\begin{cases}
\frac{(-1)^{\frac{\beta}{2}}}{2^{\alpha+\beta-1}} \sum_{\gamma=0}^{\left\lfloor \frac{1}{2}(\alpha+\beta-1) \right\rfloor} \sum_{\epsilon=\max\{\gamma-\alpha,0\}}^{\min\{\gamma,\beta\}} (-1)^{\epsilon} \binom{\alpha}{\gamma-\epsilon} \binom{\beta}{\epsilon} \cos\left[(\alpha+\beta-2\gamma)\phi\right] & \text{for } \beta \text{ even} \\
\frac{(-1)^{\frac{\beta-1}{2}}}{2^{\alpha+\beta-1}} \sum_{\gamma=0}^{\left\lfloor \frac{1}{2}(\alpha+\beta-1) \right\rfloor} \sum_{\epsilon=\max\{\gamma-\alpha,0\}}^{\min\{\gamma,\beta\}} (-1)^{\epsilon} \binom{\alpha}{\gamma-\epsilon} \binom{\beta}{\epsilon} \sin\left[(\alpha+\beta-2\gamma)\phi\right] & \text{for } \beta \text{ odd}
\end{cases}
$$

$$
+ \frac{1}{2^{\alpha+\beta}} \binom{\alpha}{\frac{\alpha}{2}} \binom{\beta}{\frac{\beta}{2}} + \frac{(-1)^{\frac{\beta}{2}}}{2^{\alpha+\beta-1}} \sum_{\epsilon=\max\left\{\frac{1}{2}(\beta-\alpha),0\right\}}^{\frac{\beta-1}{2}} (-1)^{\epsilon} \binom{\alpha}{\frac{1}{2}(\alpha+\beta)-\epsilon} \binom{\beta}{\epsilon} \quad \text{if } \alpha, \beta \text{ even.} \tag{A 15}
$$

A.2. *Harmonic as a product of sinusoids*

Here, we derive the reverse operation, expressing a harmonic as a product of sinusoids at the fundamental frequency. For $n \in \mathbb{Z}_{\geqslant 0}$, de Moivre's theorem states

$$\cos(n\phi) + \mathrm{i}\sin(n\phi) = (\cos\phi + \mathrm{i}\sin\phi)^{n}, \tag{A 16}$$

which we expand using the binomial theorem,

$$\cos(n\phi) + \mathrm{i}\sin(n\phi) = \sum_{\alpha=0}^{n} \mathrm{i}^{\alpha} \binom{n}{\alpha} \cos^{n-\alpha}\phi \, \sin^{\alpha}\phi. \tag{A 17}$$

Firstly, taking the real part, which only has contributions for even α, and letting $\beta = \frac{\alpha}{2}$ gives

$$\cos(n\phi) = \sum_{\beta=0}^{\frac{n}{2}} (-1)^{\beta} \binom{n}{2\beta} \cos^{n-2\beta}\phi \, \sin^{2\beta}\phi. \tag{A 18}$$

Secondly, taking the imaginary part, which only has contributions for odd α, and letting $\beta = \frac{\alpha-1}{2}$ gives

$$\sin(n\phi) = \sum_{\beta=0}^{\frac{n-1}{2}} (-1)^{\beta} \binom{n}{2\beta+1} \cos^{n-2\beta-1}\phi \, \sin^{2\beta+1}\phi. \tag{A 19}$$

Appendix B. Expression for infinite sum raised to integer power

In equation (5.8), we expressed an infinite power series raised to a finite integer power as a new power series,

$$\left(\sum_{s=0}^{\infty} a^{s} h_{s+1} \right)^{q} = \sum_{s=0}^{\infty} a^{s} c_{s}, \tag{B 1}$$

with the coefficients c_s to be determined. We will find a recurrence relation for c_s by first letting

$$g(a) = \sum_{s=0}^{\infty} a^{s} h_{s+1} \qquad \text{and} \qquad f(a) = (g(a))^{q} = \sum_{s=0}^{\infty} a^{s} c_{s}, \tag{B 2a}$$

whose derivatives are, where $\epsilon = \xi + 1$,

$$\frac{\mathrm{d}g}{\mathrm{d}a} = \sum_{s=0}^{\infty} s a^{s-1} h_{s+1} = \sum_{p=0}^{\infty} a^{p} (p+1) h_{p+2} \qquad \text{and} \qquad \frac{\mathrm{d}f}{\mathrm{d}a} = \sum_{s=0}^{\infty} a^{s} (s+1) c_{s+1}. \tag{B 2b}$$

We seek an equation relating different elements in the sequence c_s by differentiating $f(g(a))$ using the chain rule,

$$\frac{\mathrm{d}f}{\mathrm{d}a} = qg^{q-1}\frac{\mathrm{d}g}{\mathrm{d}a}, \tag{B 3}$$

which we multiply by g and recall that $f = g^q$ to yield

$$\frac{\mathrm{d}f}{\mathrm{d}a}g = qf\frac{\mathrm{d}g}{\mathrm{d}a}. \tag{B 4}$$

Both sides are a product of two summations, which we evaluate using the Cauchy product of power series,

$$\left(\sum_{s=0}^{\infty} a^s X_s\right)\left(\sum_{p=0}^{\infty} a^p Y_p\right) = \sum_{s=0}^{\infty} a^s \sum_{p=0}^{s} X_p Y_{s-p}, \tag{B 5}$$

on the power series forms for f, g and their derivatives (B 2) to give

$$\sum_{s=0}^{\infty} a^s \sum_{p=0}^{s} (p+1)c_{p+1}h_{s-p+1} = q\sum_{s=0}^{\infty} a^s \sum_{p=0}^{s} c_p(s-p+1)h_{s-p+2}. \tag{B 6}$$

We now observe that this equation still holds if we change the lower limit of the p summation on the left hand side to $p = -1$ without changing the summand, because the extra term that is introduced is equal to zero. Taking the terms at ord(a^s), we let $r = p + 1$, sum from $r = 0$ (rather than $r = 1$) on the left hand side and separate the term involving c_{s+1} to obtain

$$(s+1)c_{s+1}h_1 + \sum_{r=0}^{s} rc_r h_{s-r+2} = q\sum_{p=0}^{s}(s-p+1)c_p h_{s-p+2}. \tag{B 7}$$

Rearranging this equation gives the recurrence relation (5.9). The seed of the sequence of coefficients, c_0, is found by setting $a = 0$ in the power series (B 1), which gives $c_0 = h_1^q$.

Appendix C. Strongly nonlinear approach to expanding $h(x, t)$

We can derive the monochromatic expansion (5.15) by substituting for ψ (5.1) in the unexpanded kinematic boundary condition (2.16). Using the calculated derivatives of $\hat{\psi}$ (5.15*b*), but remembering to evaluate them at $z = h$ rather than $z = 0$, gives

$$-\frac{a\omega}{k}\left(1 - \tan\Theta\frac{\partial h}{\partial x}\right)\cos\left[k(x - h\tan\Theta) - \omega t\right] = \frac{\partial h}{\partial t}. \tag{C 1}$$

There is no known closed-form solution to this strongly nonlinear equation where the dependent variable, h, appears both inside and outside a trigonometric function. Instead, we expand the cosine using its compound angle formula,

$$-\frac{a\omega}{k}\left(1 - \tan\Theta\frac{\partial h}{\partial x}\right)\Big[\cos(kx-\omega t)\cos(kh\tan\Theta) + \sin(kx-\omega t)\sin(kh\tan\Theta)\Big] = \frac{\partial h}{\partial t}, \tag{C 2}$$

substitute for the horizontal phase velocity, $\phi = kx - \omega t$, and Taylor expand the trigonometric functions of h about zero to obtain polynomials in h,

$$
\begin{aligned}
-\frac{a\omega}{k}\left(1 - \tan\Theta\frac{\partial h}{\partial x}\right)\Bigg[& \cos\phi \sum_{q\ \text{even},\ \geqslant 0} \frac{(-1)^{\frac{q}{2}}}{q!}(kh\tan\Theta)^q \\
& + \sin\phi \sum_{q\ \text{odd},\ \geqslant 1} \frac{(-1)^{\frac{q-1}{2}}}{q!}(kh\tan\Theta)^q \Bigg] = \frac{\partial h}{\partial t}.
\end{aligned}
\tag{C 3}
$$

On comparison with the period pattern of the derivatives of $\hat{\psi}$ (5.15*b*), we see that the summed quantities are derivatives of $\hat{\psi}$, so we combine the summations,

$$
a\left(1 - \tan\Theta\frac{\partial h}{\partial x}\right)\sum_{q=0}^{\infty}\frac{h^q}{q!}\left.\frac{\partial^{q+1}\hat{\psi}}{\partial x\,\partial z^q}\right|_{z=0} = \frac{\partial h}{\partial t}. \tag{C 4}
$$

This Taylor's expansion of trigonometric functions matches that of Taylor expanding $\hat{\psi}$ about $z = 0$ (2.17) (remembering that $\frac{\partial}{\partial z} = -\tan\Theta\frac{\partial}{\partial x}$ in this monochromatic case), demonstrating that these two methods are equivalent. In addition, we note that the Taylor's expansions of sines and cosines have infinite radius of convergence, so this equation still holds for h of any magnitude. Restricting h to small amplitudes and substituting its expansion in powers of a (5.3) yields our expansion of the kinematic boundary condition (5.7). Finally, following the same manipulations of the summations as before, we recover our expansion grouped in powers of a (5.15).

REFERENCES

Bourget, Baptiste, Dauxois, Thierry, Joubaud, Sylvain & Odier, Philippe 2013 Experimental study of parametric subharmonic instability for internal plane waves. *J. Fluid Mech.* **723**, 1–20.

Clark, Heather A. & Sutherland, Bruce R. 2010 Generation, propagation, and breaking of an internal wave beam. *Phys. Fluids* **22** (7), 1–16.

d'Alembert 1747 Recherches sur la courbe que forme une corde tenduë mise en vibration. *Hist. l'académie R. des Sci. belles lettres Berlin* **3**, 214–219.

Dalziel, Stuart B., Hughes, Graham O. & Sutherland, Bruce R. 1998 Synthetic schlieren. In *Proc. 8th Int. Symp. Flow Vis.*.

Dalziel, S B, Hughes, G O & Sutherland, B R 2000 Whole-field density measurements by 'synthetic schlieren'. *Exp. Fluids* **28** (4), 322–335.

Dalziel, Stuart B., Patterson, Michael D., Caulfield, C. P. & Le Brun, Stéphane 2011 The structure of low-Froude-number lee waves over an isolated obstacle. *J. Fluid Mech.* **689**, 3–31.

Dalziel Research Partners 2018 DigiFlow vv3.6.0–4.2.0. http://www.dalzielresearch.com/digiflow/.

Dobra, Thomas Edward 2018 Nonlinear Interactions of Internal Gravity Waves. PhD thesis, University of Bristol.

Dobra, Thomas E., Lawrie, Andrew G. W. & Dalziel, Stuart B. 2019 The magic carpet: an arbitrary spectrum wave maker for internal waves. *Exp. Fluids* **60** (11), 172.

Egbert, Gary D. & Ray, Richard D. 2001 Estimates of M_2 tidal energy dissipation from TOPEX/Poseidon altimeter data. *J. Geophys. Res. Ocean.* **106** (C10), 22475–22502.

Ermanyuk, E. V. 2000 The use of impulse response functions for evaluation of added mass and damping coefficient of a circular cylinder oscillating in linearly stratified fluid. *Exp. Fluids* **28** (2), 152–159.

Ermanyuk, E. V., Flór, J. B. & Voisin, B. 2011 Spatial structure of first and higher harmonic internal waves from a horizontally oscillating sphere. *J. Fluid Mech.* **671**, 364–383.

Ermanyuk, E. V., Shmakova, N. D. & Flór, J. B. 2017 Internal wave focusing by a horizontally oscillating torus. *J. Fluid Mech.* **813**, 695–715.

Fortuin, J. M. H. 1960 Theory and application of two supplementary methods of constructing density gradient columns. *J. Polym. Sci.* **44**, 505–515.

Gostiaux, Louis, Didelle, Henri, Mercier, Stephane & Dauxois, Thierry 2007 A novel internal waves generator. *Exp. Fluids* **42** (1), 123–130.

Gradshteyn, I. S. & Ryzhik, I. M. 2014 *Table of Integrals, Series, and Products*, 8th edn. Academic Press.

van Haren, Hans, Maas, Leo & van Aken, Hendrik 2002 On the nature of internal wave spectra near a continental slope. *Geophys. Res. Lett.* **29** (12), 57.

Hurley, D. G. 1972 A general method for solving steady-state internal gravity wave problems. *J. Fluid Mech.* **56** (4), 721–740.

McEwan, A. D. 1973 Interactions between internal gravity waves and their traumatic effect on a continuous stratification. *Boundary-Layer Meteorol.* **5** (1-2), 159–175.

Mercier, Matthieu J., Garnier, Nicolas B. & Dauxois, Thierry 2008 Reflection and diffraction of internal waves analyzed with the Hilbert transform. *Phys. Fluids* **20**, 086601.

Mercier, Matthieu J., Martinand, Denis, Mathur, Manikandan, Gostiaux, Louis, Peacock, Thomas & Dauxois, Thierry 2010 New wave generation. *J. Fluid Mech.* **657**, 308–334.

Mowbray, D. E. & Rarity, B. S. H. 1967 A theoretical and experimental investigation of the phase configuration of internal waves of small amplitude in a density stratified liquid. *J. Fluid Mech.* **28** (1), 1–16.

Nikurashin, Maxim & Ferrari, Raffaele 2013 Overturning circulation driven by breaking internal waves in the deep ocean. *Geophys. Res. Lett.* **40** (12), 3133–3137.

Oster, Gerald 1965 Density Gradients. *Sci. Am.* **213** (2), 70–76.

Pollard, R. T. 1970 On the generation by winds of inertial waves in the ocean. *Deep Sea Res. Oceanogr. Abstr.* **17** (4), 795–812.

Scorer, R. S. 1949 Theory of waves in the lee of mountains. *Q. J. R. Meteorol. Soc.* **75** (323), 41–56.

Smith, S. & Crockett, J. 2014 Experiments on nonlinear harmonic wave generation from colliding internal wave beams. *Exp. Therm. Fluid Sci.* **54**, 93–101.

Sutherland, Bruce R. 2010 *Internal Gravity Waves*. Cambridge University Press.

Sutherland, Bruce R. 2016 Excitation of superharmonics by internal modes in non-uniformly stratified fluid. *J. Fluid Mech.* **793**, 335–352.

Sutherland, B. R., Dalziel, S. B., Hughes, G. O. & Linden, P. F. 1999 Visualization and measurement of internal waves by 'synthetic schlieren'. Part 1. Vertically oscillating cylinder. *J. Fluid Mech.* **390**, 93–126.

Sveen, J. K. & Dalziel, S. B. 2005 A dynamic masking technique for combined measurements of PIV and synthetic schlieren applied to internal gravity waves. *Meas. Sci. Technol.* **16** (10), 1954–1960.

Tabaei, Ali & Akylas, T. R. 2003 Nonlinear internal gravity wave beams. *J. Fluid Mech.* **482**, 141–161.

Tabaei, Ali, Akylas, T. R. & Lamb, Kevin G. 2005 Nonlinear effects in reflecting and colliding internal wave beams. *J. Fluid Mech.* **526**, 217–243.